# PI-(3,5)$P_2$-mediated oligomerization of the endosomal sodium/proton exchanger NHE9

Surabhi Kokane[1*], Pascal F. Meier[1*], Ashutosh Gulati[1*], Rei Matsuoka[1*], Tanadet Pipatpolkai[2], Lucie Delemotte[2], David Drew[1#]

[1]Department of Biochemistry and Biophysics, Science for Life laboratory, Stockholm University, SE-106 91 Stockholm, Sweden. [2]Department of Applied Physics, Science for Life Laboratory, KTH Royal Institute of Technology, Stockholm, Sweden.

*These authors contributed equally

#Correspondence: ddrew@dbb.su.se

## Abstract

**$Na^+/H^+$ exchangers (NHE) are found in all cells to regulate intracellular pH, sodium levels and cell volume. The NHE isoform 9 (SLC9A9) fine-tunes endosomal pH, and its activity is linked to glioblastoma, epilepsy, autism spectrum and attention-deficit-hyperactivity disorders. Here, we report cryo-EM structures of *horse* NHE9 and a cysteine-variant at 3.6 and 3.1 Å resolution, respectively. We show how lysine residues, from a previously unresolved TM2-TM3 β-hairpin loop domain, are positioned above the dimerization interface and interact with the endosomal-specific PI-(3,5)$P_2$ lipid, together with residues located on dimer domain helices. Thermal-shift assays, solid-state membrane (SSM) electrophysiology and MD simulations, corroborates that NHE9 can specifically bind PI-(3,5)$P_2$, and that its addition stabilizes the homodimer and enhances NHE9 activity. We have further determined the cryo-EM structure of *E. coli* NhaA, confirming the expected coordination of cardiolipin at the dimerization interface, solidifying the concept that $Na^+/H^+$ exchanger dimerization and transporter activity can be regulated by specific lipids. Taken together, we propose that the activity of NHE9 is regulated by the PI-(3,5)$P_2$ lipid upon reaching endosomes, which we refer to as an lipid-activation-upon-arrival model.**

## Introduction

$Na^+/H^+$ exchangers (NHE) facilitate the electroneutral exchange of cations ($Na^+/Li^+/K^+$) and protons ($H^+$) across membranes to regulate intracellular pH, sodium levels and cell volume (Pedersen & Counillon, 2019). In mammals, there are 13 different isoforms belonging to the SLC9A (NHE1-9), SLC9B (NHA1-2) or sperm specific SLC9C families (Fuster & Alexander, 2014; Pedersen & Counillon, 2019). NHEs differ in their substrate preferences, kinetics, subcellular and tissue distribution (Pedersen & Counillon, 2019). Isoforms NHE1-5 are primarily expressed on the plasma membrane and have important physiological roles linked to cellular pH homeostasis (Pedersen & Counillon, 2019). Isoforms NHE6-9 are primary localized to intracellular compartments and work in concert with the V-type ATPase to fine-tune intracellular pH in their respective organelles.

NHEs are physiological homodimers (Brett *et al*, 2005; Fuster & Alexander, 2014; Pedersen & Counillon, 2019), with each monomer made up of a transporter unit and a C-terminal cytosolic tail between ~125-440 residues in length (Fuster & Alexander, 2014; Pedersen & Counillon, 2019). The mammalian transport modules share low sequence homology to bacterial $Na^+/H^+$ antiporters harbouring the "NhaA-fold", so-named after the first crystal structure obtained from *E. coli* (Brett *et al.*, 2005; Fliegel, 2019; Padan, 2008). The cryo-EM structures of NHE1 and NHE9 have been determined and nonetheless show a similar architecture to bacterial homologues with 13 transmembrane (TM) helices (Hunte *et al*, 2005; Lee *et al*, 2013; Paulino *et al*, 2014; Wohlert *et al*, 2014). The transporter unit consists of two distinct domains, a dimerization domain and an ion-transporting (core) domain. The 6-TM core domain undergoes global, elevator-like structural transitions to translocate ions across the membrane against the anchored dimerization domain (Coincon *et al*, 2016; Drew & Boudker, 2016). NHE1 is a house-keeping $Na^+/H^+$ exchanger, which is localised to the plasma membrane of most eukaryotic cells (Pedersen & Counillon, 2019). In contrast, NHE9 (SLC9A9) regulates the luminal pH of late- and recycling endosomes (Kondapalli *et al*, 2015; Kondapalli *et al*, 2014). Mutations in SLC9A9 have been associated with neurological disorders such as familial autism, ADHD and epilepsy (Kondapalli *et al.*, 2014; Zhang-James *et al*, 2019) and NHE9 expression is upregulated in glioblastoma, one of the most aggressive forms of brain cancers (Kondapalli *et al.*, 2015). NHE9 expression is also upregulated in response to viral infection (Slonchak *et*

*al*, 2019) and NHE9 variants are more frequent amongst patients who develop severe response to SARS-CoV-2 infection (Prasad, 2021).

A superimposition of the respective inward-facing structures of NHE1 and NHE9 confirms that the overall architecture is well-conserved (Fig. 1A). The main difference is that the transporter domain of NHE9 was predicted by AlphaFold 2 (AF2)(Jumper *et al*, 2021) to contain a ~ 60 residue extension of the TM2 -TM3 loop (Fig. 1B). In human NHEs, the extended loop domain sequence is present in organellar isoforms NHE7 and NHE9, as well as isoform-two of endosomal NHE6 (Supplementary Fig. 1A). Using native mass-spectrometry, we previously concluded that the NHE9 dimer co-purifies with lipid adducts of ~1KDa in size, whereas NHE9 monomers were essentially lipid-free (Winklemann *et al*, 2020). In the NHE1 nanodisc structure, aliphatic parts of fatty acids could be modelled at the dimerization interface (Fig. 1A) (Dong *et al*, 2021). The data quality limitation of the NHE9 structure in detergent, however, prevented the modelling of lipids at the dimer interface (Winklemann *et al.*, 2020). Nonetheless, we could detect map density for the TM2-TM3 loop, corresponding to a position above the aliphatic chains in NHE1 (Supplementary Fig. 1B). Native MS demonstrated that NHE9 co-purifies with negatively-charged phosphatidylinositol lipids matching the mass of $PIP_2$ (Winklemann *et al.*, 2020). Given the lack of positively-charged TM residues, it was hypothesized that the TM2-TM3 loop domain would help to coordinate the negatively-charged lipid head-groups. Consistently, the mutation of two lysine residues Lys105 and Lys107 in the unresolved TM2-TM3 loop domain, was sufficient to abolish $PIP_2$ stabilization and, under native MS conditions, the mutant was detected as a lipid-free monomer (Winklemann *et al.*, 2020). Here, we set out to resolve a cryo-EM structure of NHE9 with the TM2-TM3 loop domain to understand its role in lipid-mediated regulation.

## Results

*Solid-supported membrane (SSM) electrophysiology of horse NHE9**

Previously, NHE9 from *horse* was selected for cryo-EM studies as it was found to be more detergent stable than *human* NHE9 (Winklemann *et al.*, 2020). Purified *horse* NHE9* (residues 8 to 574; out of 645) was reconstituted into liposomes together with $F_0F_1$-ATP synthase for proteoliposome studies and an apparent $K_M$ of NHE9* for $Na^+$ of 20.5 ± 3 mM was determined (Winklemann *et al.*, 2020). However, a high

background from empty liposomes made studies of NHE9* activity challenging, as the signal-to-noise ratio was low ~ 3:1. More recently, we have used solid-supported membrane (SSM) electrophysiology to record $Na^+$ translocation of the mammalian $Na^+/H^+$ exchanger NHA2 (Matsuoka *et al*, 2022). In brief, proteoliposomes are adsorbed to an SSM and charge translocation is measured *via* capacitive coupling of the supporting membrane, following accumulation of transported ions (Bazzone *et al*, 2017). Here, to put the kinetic estimates for NHE9 on a firmer footing, we recorded SSM-data for NHE9* proteoliposomes upon increasing concentrations of $Na^+$ (Fig. 1D). Peak currents were ~6-fold higher than either the NHE9* variant for which ion-binding site residues Asn243 and Asp244 were substituted to alanine, or a mammalian transporter for fructose (GLUT5) (Fig. 1C). The estimated binding affinity ($K_d$) determined by SSM for $Na^+$ is 36.3 ± 4 mM, which is similar to the Michaelis–Menten $K_M$ estimate for NHE9* in proteoliposomes (Supplementary Fig. 1D)(Winklemann *et al.*, 2020). Thus, we can confirm that NHE9* has binding affinity for sodium at a similar concentration range to the *in vivo* $K_M$ estimates measured for other intracellular localized NHE6 and NHE8 isoforms (Pedersen & Counillon, 2019).

*Cryo-EM structure of NHE9* with TM2-TM3 β-loop domain at low pH 6.5*

The previous *horse* NHE9* cryo-EM structure was determined from protein purified in the detergents LMNG and CHS and in buffer at pH 7.5 (Winklemann *et al.*, 2020). We attempted to improve the quality of the cryo-EM maps by incorporation of NHE9* into nanodiscs, but saw no significant improvement in the final map quality, when comparing to maps from the detergent samples (results not shown). As a next approach, we repeated the collection of NHE9* in detergent, but buffered to pH 6.5 where NHE9 is thought to be less active, and therefore presumably less dynamic. Overall, we collected ~4,300 movies and the final 3D-reconstruction contained data of 244,000 particles, from which an EM map could be reconstructed to 3.3 Å according to the gold-standard Fourier shell correlation (FSC) 0.143 criterion (Supplementary Fig. 2). Comparison of the NHE9* structures determined at pH 7.5 and pH 6.5 showed no apparent differences (Supplementary Fig. 1E). We speculated that the respective final 3D reconstructions may still contain heterogeneity and we therefore performed 3D-variability analysis in CryoSPARC (Punjani *et al*, 2017), followed by clustering (principal component) analysis to separate further classes. Selecting 40% of the

particles for heterogeneous refinement, enabled an improved cryo EM map reconstruction of NHE9* at pH 6.5, with additional map features for the TM2-TM3 loop domain (Supplementary Fig. 3). Further homogenous refinement with C2 symmetry improved the cryo EM density for the TM2-TM3 loop domain with an overall resolution of 3.6 Å (Supplementary Fig. 3A). As a last-step, a composite map was generated for model building, combining the additional TM2-TM3 loop domain features with the higher resolution EM maps (Supplementary Fig. 3B).

Previously, we modelled the TM2-TM3 loop domain of NHE9* based on several structure prediction algorithms that detected the sequence homology to the β-hairpins in *E. coli* NhaA (Supplementary Fig. 1C) (Lee *et al*, 2014; Winklemann *et al.*, 2020). Consistently, the AF2 model of NHE9 predicts β-hairpins in the TM2-TM3 loop domain with a high confidence score (Jumper *et al.*, 2021), but has a low confidence score for the regions connecting the β-hairpins with extracellular ends of TM2 and TM3 (Fig. 1B). The AF2 prediction of the NHE9 monomer superimposes well with the NHE9* structure (Supplementary Fig. 4A). The AF2 dimer model is also similar to the AF2 monomer model, apart from the β-hairpin (Supplementary Fig. 4A), which is now modelled to interact with the β-hairpin from its neighbouring protomer (Fig. 1E, Methods). Subsequently, we refined the AF2 NHE9 dimer model into the NHE9* cryo-EM maps with some further manual adjustment where needed (Methods and Fig. 1F). At the extracellular end of TM2, a flexible loop, residues Pro72 to Asp82, were predicted by AF2 as extending towards the centre of the dimerization interface, followed by short-linker and a β-hairpin strand that is angled 60° away from the NHE9* surface (Fig. 1B, E). Based on the cryo EM maps at ~ 4.0 Å resolution (Supplementary Fig. 3A), we were able confidently refine the overall position of the short linker and β-hairpin strand, but map density was insufficient to support some side-chains positioning or the flexible loop (Fig. 1F). The β-hairpin strand loops back to the beginning of TM3 and contain a bent helix, annotated as extracellular helix (ECH1), which is well supported by the cryo EM maps (Fig. 1F). The β-hairpins are predicted by AF2 to be domain-swapped, and this arrangement refines well into the map density. In the middle of the loop domain, a cluster of six positively-charged residues Lys105, Lys107 and Arg108 from each of the two protomers extend towards the dimerization interface (Fig. 1F). Overall, the TM2-TM3 β-loop domain clasps the two protomers together on the

luminal side, and forms a highly positively-charged cluster that is now located above the dimerization domain interface. As such, the re-modelled NHE9* structure is consistent with its previously proposed requirement for binding negatively-charged $PIP_2$ lipids (Winklemann *et al.*, 2020).

*Cryo-EM structure of cysteine variant (NHE9*CC) shows binding of PI-(3,5)$P_2$ lipids*

In order to improve the resolution of the NHE9* structure, we substituted Leu139 and Ile444 residues in an attempt to disulphide-trap the inward-facing state. In addition, we added brain lipids during each step of the NHE9*CC purification (see Methods). We subsequently collected a larger data-set of 13,780 movies and the final 3D-reconstruction had 78,370 particles from which an EM map was reconstructed to 3.2 Å according to the gold-standard Fourier shell correlation (FSC) 0.143 criterion (Supplementary Fig. 4B). Despite the similar FSC resolution estimate, the new cryo-EM maps were improved with some local regions extending to 2.5 Å resolution (Supplementary Fig. 4B). In particular, the density was clearer for the TM2-TM3 β-loop at lower contour levels (Supplementary Fig. 4B). In NHE9*, there was no cryo EM map density for the 100-residue long C-terminal regulatory domain (CTD) (Winklemann *et al.*, 2020), likely a result of its predicted dynamics and intrinsic disorder (Hendus-Altenburger *et al*, 2014; Norholm *et al*, 2011; Pedersen & Counillon, 2019). In the improved NHE9* CC maps we could, however, model an additional 52 residues of the C-terminal regulatory domain (Fig. 2A and Supplementary Fig. 5A). A structural superimposition of the refined NHE9* CC and NHE9* structures otherwise show small differences (Supplementary Fig. 4C). Map density and sulphur atom distances did not support any disulphide bond formation between the two introduced cysteine residues (Supplementary Fig. 5B). SSM-based electrophysiology for NHE9*CC mutant confirmed that the cysteine variant binds $Na^+$ with similar affinity as NHE9* (Supplementary Fig. 1D). Currently, it's unclear whether the improved map quality for NHE9*CC is due to the introduced cysteine mutations, or by the repeated addition of lipids during purification.

At the dimerization interface we could now observe additional lipid-like features in the cryo EM maps (Fig. 2A). Rather than the cylinder-like density of fatty acids as seen in the NHE1 nanodisc structure in POPC lipids (Dong *et al.*, 2021), the cryo-EM maps show larger, head-group lipid densities with distinct features (Fig. 2A, Supplementary

Fig. 5C). Given that NHE9* co-purified from yeast with several lipids corresponding to the molecular mass of $PIP_2$ (Winklemann *et al.*, 2020), we attempted to model two $PIP_2$ molecules into the NHE9* CC maps and found that the density was a better fit for the lipid phosphatidylinositol-3,5-bisphosphate PI-(3,5)$P_2$,, rather than the more abundant lipid phosphatidylinositol-4,5-bisphosphate PI-(4,5)$P_2$ (Fig. 2A, Supplementary Fig. 5C). Although PI-(3,5)$P_2$ is a minor $PIP_2$ lipid, it is specific to late endosomes and lysosomes (Hasegawa *et al*, 2017), which overlaps with the functional localization of NHE9 (Hasegawa *et al.*, 2017). In contrast, the $PIP_2$ lipid PI-(4,5)$P_2$ is principally found in the plasma membrane (Ho *et al*, 2012). In an electrostatic surface potential map, the PI-(3,5)$P_2$ lipids could neutralise the positively-charged loop domain residues Lys105, Lys105' Lys107, Lys107' previously predicted to interact with $PIP_2$ lipids (Fig. 2A,B) (Winklemann *et al.*, 2020).

Dimerization contacts are formed between TM1 and TM8' of the neighbouring protomer. The glycerol backbone and connecting acyl chains of each PI-(3,5)$P_2$ lipid forms hydrophobic stacking interactions to Trp321 (TM8, TM8') and its indole nitrogen interacts with the phosphodiester (Fig. 2A). The glutamate residue Glu23 (TM1, TM1'), further hydrogen bonds to the C5-OH of the *myo*-inositol sugar and also stabilises a likely water-mediated sugar interaction. The position of Glu23 could partially explain the preference for PI-(3,5)$P_2$ lipids, since a negative-charged $PO_4^{2-}$ at the C5-OH position would interact unfavourably with the carboxylate group of Glu23. Moreover, a glutamine residue Gln21 (TM1, TM1') is also well positioned to interact with the phosphomonoester in the C3-OH position, but map density was insufficient to confirm this (Fig. 2A). Overall, the hydrophobic dimerization interface, together with polar and aromatic residues located at its surface and positive-charged residues from the TM2-TM3 β-hairpin loop, create an environment well-suited for binding PI-(3,5)$P_2$ lipids (Fig. 2B).

*PI-(3,5)$P_2$ lipid binding by thermostability, electrophysiology, and MD simulations*

The cryo-EM maps of the TM2-TM3 β-hairpin loop domain in NHE9* CC were still of insufficient quality for modelling side-chains in this region (Supplementary Fig. 4B), likely due to inherent flexibility. We had previously detected interactions with $PIP_2$ and $PIP_3$ lipids to NHE9* using FSEC-TS and GFP-based thermal stability assays (Nji *et*

*al*, 2018; Winklemann *et al.*, 2020), which we confirmed could monitor cardiolipin binding to the *E. coli* $Na^+/H^+$ antiporter NhaA (Landreh *et al*, 2017; Nji *et al.*, 2018). The average melting temperature ($\Delta T_m$) of NHE9* increased by 8°C with PI-(4,5)$P_2$ addition, whereas other lipids POPC, POPE and POPA showed no stabilization (Winklemann *et al.*, 2020). To validate that PI-(3,5)$P_2$ would also stabilise NHE9* in a similar manner, NHE9* GFP-TS melting curves were recorded in the presence of either PI-(4,5)$P_2$ or PI-(3,5)$P_2$ lipids (Methods and Fig. 2C). Unexpectedly, NHE9* show greater thermostabilization in the presence of PI-(3,5)$P_2$, with a $\Delta T_m$ of 15°C, as compared to $\Delta T_m$ of 8°C for PI-(4,5)$P_2$. Moreover, NHE9* starts to unfold around 30°C with a shallow slope for the transition temperature, which is indicative of a mixed protein population (Fig. 2C). In contrast, with PI-(3,5)$P_2$ added, NHE9* melts with a sharp transition, consistent with the shift to a single oligomeric population (Fig. 2C). Using FSEC we could confirm that a higher fraction of detergent-purified NHE9* dimer is retained if PI-(3,5)$P_2$ lipid was added prior to heating at 50ºC for 10 mins, as compared to either PI-(4,5)$P_2$ or PC lipid addition (Supplementary Fig. 6A). We had previously shown that substitution of TM2-TM3 lysine residues to glutamine in NHE9* (Lys85Gln-Lys105Gln-Lys107Gln) abolished PI-(4,5)$P_2$ stabilization and oligomerization by native MS (Winklemann *et al.*, 2020). Indeed, the NHE9* (Lys85Gln-Lys105Gln-Lys107Gln) variant purified as a monomer in detergent, and the addition of either PI-(3,5)$P_2$, PI-(4,5)$P_2$ or PC lipids showed only minimal thermostabilization (Supplementary Fig. 6B-C). Taken together, thermostability-shift assays indicates that NHE9* has a preference for the lipid PI-(3,5)$P_2$ and its addition likely stabilises the functional homodimer.

To assess the influence of PI-(3,5)$P_2$ lipid addition to NHE9* activity, we incubated the purified NHE9* protein with either buffer, or buffer containing solubilised PI-(3,5)$P_2$ lipids, and reconstituted this mixture into liposomes made from yeast-polar lipids (Methods). SSM-based electrophysiology of NHE9* incubated with buffer produces similar peak currents upon $Na^+$ addition to those shown previously, whereas NHE9* protein incubated with PI-(3,5)$P_2$ lipid produced a stronger response to $Na^+$ addition (Fig. 2D, E and Supplementary Fig. 1D), and showed an four-fold increase in its binding affinity for $Na^+$ ($K_d$ = 9.6 mM) (Supplementary Fig. 6E). In contrast, the PI-(4,5)$P_2$ lipid addition had a similar $Na^+$ binding affinity as the buffer only addition to NHE9*

(Supplementary Fig. 6E). To confirm that the response to PI-(3,5)$P_2$ was likely mediated by the expected interaction with the lysine residues in the TM2-TM3 β-hairpin loop domain, we recorded SSM-based currents for the purified lysine-to-glutamine NHE9* (Lys85Gln-Lys105Gln-Lys107Gln) variant. The triple glutamine variant also showed a weaker affinity for $Na^+$ ($K_d$ = 55 mM) compared with NHE9* and, in fact, the addition of the PI-(3,5)$P_2$ lipid decreased its apparent affinity for $Na^+$ ($K_d$ = 88 mM) (Supplementary Fig. 6E). The outside surface of the PI-(3,5)$P_2$-stabilised NHE9* TM2-TM3 β-hairpin loop domain has a partially negatively-charged surface (Fig. 2B). It is possible that stabilization of the TM2-TM3 β-hairpin loop domain by PI-(3,5)$P_2$ lipids provides an electrostatic pathway that can better attract ions to the outward-facing funnel.

To evaluate if that the lysine residues in the TM2-TM3 β-hairpin loop domain could interact with $PIP_2$ lipids, we carried out molecular dynamics (MD) simulations of the NHE9* structure and a *in silico* modelled NHE9* (Lys85Gln-Lys105Gln-Lys107Gln) variant (see Methods). In the simulations using the NHE9* structure, the PI-(3,5)$P_2$ lipid stayed within less than 3 Å from its initial position for nearly the entire simulation time (Fig. 3A,B). In contrast, a modelled PI-(4,5)$P_2$ lipid was less stably bound with a higher fraction of frames showing > 3 Å movement from its initial position (Fig. 3B). The distribution of salt-bridge interactions with Lys105 and Lys107 residues revealed that Lys105 residues were nearly always in contact with the PI-(3,5)$P_2$ lipid, whereas Lys107 residues remained in contact for around half of the simulation time (Fig. 3C,E). The PI-(4,5)$P_2$ lipid had a much larger variation for interaction with the lysine residues and the preferred interaction with Lys105 was less pronounced (Fig. 3D, E). In MD simulations of the modelled NHE9*(Lys85Gln-Lys105Gln-Lys107Gln) variant, neither of the $PIP_2$ lipids were stably bound and the lipids had no clear interaction with the modelled glutamines (Fig. 3B-D). Overall, the MD simulations support that lysine residues in the TM2-TM3 β-hairpin loop can form stable interactions with the modelled PI-(3,5)$P_2$ lipids observed in the NHE9*CC variant.

*Cryo EM structure of NhaA confirms cardiolipin binding at the dimerization interface*

Whilst modulation of transporter activity, through means of lipid-dependent oligomerization might seem unorthodox, the formation of the functional homodimer of

the bacterial $Na^+/H^+$ antiporter NhaA from *E. coli* has previously been shown to be dependent on the negatively-charged lipid cardiolipin (Landreh *et al.*, 2017; Nji *et al.*, 2018; Quick *et al*, 2021; Rimon *et al*, 2019). Since cardiolipin synthesis in *E. coli* is increased upon salt-stress and, because NhaA is required to alleviate salt-stress (Padan, 2008; Romantsov *et al*, 2009), there is a precedence for negatively-charged lipids regulating the activity of $Na^+/H^+$ exchangers. Comparing structures of bacterial $Na^+/H^+$ exchangers that bind cardiolipin to those that do not, have shown that the sensitivity to this lipid is matched with structural differences in their oligomeric interfaces (Gupta *et al*, 2017; Nji *et al.*, 2018).

NhaA has become a model system for the lipid-dependent oligomerization of $Na^+/H^+$ exchangers and yet, we have no structural data confirming the coordination of cardiolipin at the dimerization interface of NhaA. Hence, from grids of detergent-purified NhaA, a data-set of 14,329 movies was collected and yielded an EM map reconstructed to 3.37 Å according to the gold-standard Fourier shell correlation (FSC) 0.143 criterion (Supplementary Fig. 7). As expected from native MS and MD simulations (Gupta *et al.*, 2017), thermal-shift assays (Nji *et al.*, 2018), and functional activity analysis (Quick *et al.*, 2021; Rimon *et al.*, 2019) clear map density to support the modelling of cardiolipin at the dimerization interface was observed (Fig. 4A, B). One CDL was present in the middle of the positively-charged dimerization interface, and two additional CDL lipids bind on either outside surface of the dimer interface (Fig. 4A, B). Although the dimerization interface is very positively-charged with four arginine residues per protomer — Arg203, Arg204, Arg245 and Arg250 — only the Arg204 residue directly interacts with the phosphate headgroups of CDL, and Thr205 hydrogen bonds to the oxygen atom of the distal phosphoester bonds (Fig. 4C, D). Deeper in the pocket, the side chain of Trp258 interacts with both the central and the flanking CDL molecules, where the side-chain is sandwiched between the distal glycerol moieties of the CDL lipids, forming hydrophobic stacking interactions with the acyl chains. This coordination of CDL is entirely consistent with computational analysis of CDL binding sites from analysis of more than 40 different *E. coli* proteins (Corey *et al*, 2021). Moreover, we have previously shown that an Arg203Ala and Arg204Ala double-mutant abolished thermostabilization of NhaA by CDL (Winkelmann *et al*, 2022). We have previously shown that between pH 4 and pH 6.5

the inward-facing cavity of NhaA opens up to allow $Na^+$ entry (Winkelmann *et al.*, 2022). The homodimer structure of NhaA at pH 7.5 also shows an open inward-facing cavity like the NhaA monomeric crystal structure at pH 6.5 (Fig. 4E). Taken together, we have been able to confirm the coordination of CDL binding to the NhaA homodimer, representing its most native structural conformation seen to date.

*Further mechanistic insights from the improved cryo-EM NHE9 CC* structure*

A detailed mechanistic model for ion-exchange in NHE proteins is yet to be established, as the coordination geometry of the transported $Na^+$ is unknown. Whilst molecular dynamic simulations and biochemical and biophysical approaches have provided an important framework in the bacterial exchangers (Alhadeff & Warshel, 2015; Arkin *et al*, 2007; Huang *et al*, 2016; Kozachkov & Padan, 2013; Paulino & Kuhlbrandt, 2014), a detailed understanding of the mammalian NHE's require an accurate model for the position of the ion-binding sites. In the improved NHE9*CC maps, we were able to confidently model all side-chains forming the ion-binding site, which are positioned around the half-helical cross-over (Fig. 5A and B). We observed some minor differences between the side-chain positions of Thr214, Asp215, Glu239 and Arg408 from the previously reported NHE9* structure (Winklemann *et al.*, 2020), and also between NHE9 and NHE1 (Fig. 5B, C). In MD simulations of NHE9 it was observed that $Na^+$ can be coordinated within the core domain forming interactions to Asp244, Asn243 Ser240 and Thr214 and several waters (Winklemann *et al.*, 2020). Based on phylogenic analysis (Masrati *et al*, 2018), it was predicted that a salt-bridge would also form between Glu239 in TM6 and Arg408 in TM11, but previous NHE9 and NHE1 models were inconclusive, due to insufficient map density in this region.

Here, we can confirm a salt-bridge is indeed formed between Glu239 and Arg408 residues and given the position of Glu239 in the ion-binding site, we propose this salt-bridge aids the stabilization of the residues required for coordinating $Na^+$ binding (Fig. 5C). Interestingly, Thr214 forms a parallel hydrogen bond to the ion-binding residue Asn243 (Fig. 5C). This unexpected hydrogen bond establishes a more rigid ion-binding site than that observed in NHE1, since the Thr214 residue is replaced by valine in NHE1 (Fig. 5B, C). Indeed, all the plasma membrane localized NHE isoforms have a hydrophobic residue in this position, whereas the intracellular isoforms have a

threonine residue (Winklemann *et al.*, 2020). It seems likely that this structural difference might be the reason why intracellular isoforms are thought to be able to transport $K^+$ in addition to $Na^+$ (Donowitz *et al*, 2013; Pedersen & Counillon, 2019).

In NHE proteins, extrinsic factors bind to a large, intracellular C-terminal regulatory domain of ~125 – 440 amino acids, which is only found in the mammalian proteins (Brett *et al.*, 2005; Donowitz *et al*, 2009; Fuster & Alexander, 2014; Orlowski & Grinstein, 2004). The regulatory domain is partly structured and is predicted to be less ordered towards the distal end (Donowitz *et al.*, 2009; Norholm *et al.*, 2011). In NHE1, removal of the regulatory domain results in a constitutionally active transporter (Wakabayashi *et al*, 1992). The C-terminal domain has been referred to as an allosteric regulatory subunit, which influences ion-exchange activity *via* interaction with many effectors (Lacroix *et al*, 2004) e.g., calmodulin (CaM), calcineurin B-homologous protein (CHP) and others (Donowitz *et al.*, 2013; Donowitz *et al.*, 2009; Norholm *et al.*, 2011; Odunewu-Aderibigbe & Fliegel, 2014; Slepkov *et al*, 2007). The interactions of many of these effectors are dynamic, and can further modulate activity through multiple phosphorylation sites that leads to the recruitment of other factors leading to both up and down-stream signaling as well as trafficking (Donowitz *et al.*, 2009). Although, it is well-established that these interactions are important to NHE physiology, the molecular details are just emerging.

The recent human NHE1 structure in complex with CHP1 revealed an interaction with an interfacial α-helical stretch formed by residues 517 to 539 (Dong *et al.*, 2021). Unexpectedly, the CHP1 interacting with the interfacial helix was found to have no direct contacts with the transporter module itself, and is currently unclear how CHP1 binding increases NHE1 activity (Dong *et al.*, 2021). Key to developing an allosteric model for extrinsic regulation is to obtain an NHE structure without complex partners. In the improved NHE9*CC structure, we could model part of the C-terminal domain without protein complex partners and, despite low sequence identity to NHE1 (Winklemann *et al.*, 2020), we could model the interfacial helix aligning well with the position of the interfacial helix of NHE1 (Fig. 6). The interfacial helix in the CTD sits on the membrane interface and wraps around from the core domain to the linker helix TM7 (Fig. 6A and Supplementary Fig. 9). In particular, the highly-conserved Lys301 on the linker helix makes direct hydrogen bond interactions to Thr541 and backbone carbonyl oxygens, facilitated by a proceeding proline residue (Fig. 6A, B and

Supplementary Fig. 8).

Given that the NHE1 and NHE9 structures superimpose well, apart from the position of the interfacial helix, it seems likely that the binding of CHP1 to the loop region, proceeding the interfacial helix, has driven its dissociation from the linker helix (Fig. 6C). Consistently, the AF2 model of NHE1 is similar to the NHE9 with interactions between TM7 and the CTD (Fig. 6D). The cytoplasmic surface is also more positively charged with the CTD helix in the likely inhibited position, which could diminish the attraction of positively-charged ions to the inward-facing cavity (Supplementary Fig. 9B-C).

We did not observe any map density for the 20-residue loop region proceeding the interfacial helix in NHE9* CC and has been currently modelled by AF2 (Fig. 2A); this loop is likely too dynamic in the absence of a binding partners, since half of the residues are charged. Given the TM7 linker helix undergoes significant rearrangements between outward and inward-facing states (Coincon *et al.*, 2016), we propose that the NHE9 activity is inhibited because the C-terminal helix restricts its mobility, thereby restricting core domain movement. However, the binding of CHP1 likely removes this physical constraint to enhance NHE9 activity (Fig. 6C). This autoinhibitory allosteric model would be consistent with the fact the removal of the C-terminal tail in NHE1 results in a constitutional active transporter (Donowitz *et al.*, 2013; Pedersen & Counillon, 2019; Wakabayashi *et al*, 1997). Notably, the surface of the interfacial helix and proceeding loop is positively-charged and also harbors two histidine residues His533 and His542 (Fig. 6A). It's possible that the mobility of the C-terminal tail would further be influenced by pH and the binding of negatively-charged phosphatidylinositol lipids to this region (Aharonovitz *et al*, 2000; Shimada-Shimizu *et al*, 2014), as proposed for NHE1 and NHE3 proteins (Pedersen & Counillon, 2019).

## Discussion

The mammalian NHE proteins are overall similar to the basic architecture defined by the bacterial homologues with 13-TMs (Winklemann *et al.*, 2020). Cryo EM structure of the plasma membrane localised isoform NHE1 and the endosomal isoform NHE9* superimpose well (Dong *et al.*, 2021; Winklemann *et al.*, 2020), but with some important structural differences revealed here. Although cell surface expression of NHE9 is possible in mutant cell lines, NHE9 in the plasma membrane has shown to

have no detectable activity (Daniel Fuster, *personal communication*). Expression of the intracellular NHE7 on the cell surface also results in a poor affinity for $Na^+$ ($K_M$ at 240 mM) and no activity for $K^+$ (Milosavljevic *et al*, 2014; Pedersen & Counillon, 2019), which is in contrast with the proposed activity of intracellular NHE7 and other members for $K^+$ (Lin *et al*, 2005; Nakamura *et al*, 2005). Since intracellular NHEs recycle through the plasma membrane they could, in principle, acidify vesicles upon exposure to high $Na^+$ levels, and yet vesicular acidification in NHE7-expressing cells has not been detectable (Milosavljevic *et al.*, 2014). The mechanistic basis for keeping them inactive during plasma membrane recycling has been puzzling. Here, we have been able to obtain cryo-EM maps of NHE9 that has enabled the refinement of a positively-charged TM2-TM3 β-hairpin loop domain. The cryo-EM structure and functional analysis, demonstrates that charged residues in the loop domain and polar residues in TM1 and TM8 dimer domain helices, are well positioned to interact with the minor PI-(3,5)$P_2$ lipid, rather than the more abundant PI-(4,5)$P_2$ lipid specific to the plasma membrane. Although unexpected, PI-(3,5)$P_2$ is a minor lipid that is not found in the plasma membrane, but only found in late endosomes and lysosomes (Hasegawa *et al.*, 2017; Ho *et al.*, 2012), which coincides with the localization of NHE9. Furthermore, PI-(3,5)$P_2$ lipid is increased 20-fold upon osmoregulation and salt-stress (Dove *et al*, 1997; Hasegawa *et al.*, 2017), which are conditions that also increases expression of yeast $Na^+/H^+$ exchangers (Pedersen & Counillon, 2019). Moreover, the V-type ATPase is known to co-localise with NHE9, and work together to fine-tune organellular pH (Kondapalli *et al.*, 2015). Consistent with the proposed model, the activity of the V-type ATPase is also increased in the presence of PI-(3,5)$P_2$ lipids (Li *et al*, 2014). Lastly, inhibition of enzymes required to produce PI-(3,5)$P_2$ lipids results in impaired epidermal growth factor receptor (EGFR) trafficking (de Lartigue *et al*, 2009). Indeed, NHE9 activity has been shown to be critical for EGFR sorting and turnover (Kondapalli *et al.*, 2015).

The sequence for the β-hairpin TM2-TM3 loop domain is absent in the plasma membrane NHE isoforms, which adds support this structural-feature has evolved as an additional, regulatory element. Interestingly, the closely-related NHE6 isoform has the TM2-TM3 loop domain present in most organisms, including the great apes, but in human its only present in isoform two (Supplementary Fig.1A). A lipid-activated model by dimerization through an endosomal lipid could further explain the poor and/or absent

activity for NHE7 and NHE9 proteins measured at the plasma membrane in mutant cell lines. Indeed, the increased $Na^+$ binding ($K_d$) affinity from 36 to 9 mM in the presence of PI-(3,5)$P_2$ would be more consistent with NHE9 utilizing cytoplasmic $Na^+$ in neurons, which is reported to be around 15 mM (Kondapalli *et al*, 2013). To provide additional support for lipid-dependent oligomerization in $Na^+/H^+$ exchangers we determined the cryo-EM structure of *E. coli* NhaA homodimer, confirming the expected coordination of lipids at the dimerization interface. In an analogous manner to PI-(3,5)$P_2$, the negatively-charged cardiolipin lipid head-groups bind between positively charged residues located at the dimerization interface (Nji *et al.*, 2018).

More recently, the cryo EM structure of *bison* $Na^+/H^+$ exchanger NHA2 was determined and it was shown that it has an additional TM helix at the N-terminus, as compared to the NHE9 and related 13-TM members (Matsuoka *et al.*, 2022). The N-terminal helix (TM –1) is repeat-swapped, and makes all of the dimerization contacts and, in doing so, establishes a very large, cytoplasmic opening between the two protomers. The dimerization interface buries a total surface area of only 1,000 $Å^2$, making it one of the smallest oligomeric interfaces seen for any elevator protein. Removal of the additional TM –1 helix, or the mutation of just two polar residues at the dimer interface, was enough to disrupt dimerization of NHA2 (Matsuoka *et al.*, 2022). NHA2 is well-folded as a monomer, yet mutations resulting in only the monomer were non-functional when assessed for their ability to rescue cell growth in a salt-sensitive yeast strain (Matsuoka *et al.*, 2022). This example with NHA2 clearly shows that oligomerization is essential for activity in $Na^+/H^+$ exchangers. By combining native MS with thermal-shift assays, PI lipid stabilization of the NHA2 homodimer was concluded and a cryo EM structure in nanodiscs with PI lipids showed that the cytoplasmic opening was now closed, with map density matching PI lipids at the dimerization interface (Matsuoka *et al.*, 2022). Taken together, lipid-mediated oligomerization of $Na^+/H^+$ exchanger's is becoming clear, yet the physiological basis for such regulation is just emerging. For NHE9, the binding of PI-(3,5)$P_2$ is consistent with its subcellular location, and the lipid could either enhance or completely turn on NHE9 activity by stabilizing the homodimer once it reaches late-endosomes (Fig. 7). To the best of our knowledge, such a lipid-activation-upon-arrival model would be a novel regulatory mechanism for ion-transporters and SLCs in general.

In addition to the lipid-dependent oligomerization, mammalian NHEs have a long C-terminal regulatory domain that regulates their activity (Pedersen & Counillon, 2019). The C-terminal domain is poorly conserved across the different NHE members and, so far, only part of the C-terminal tail could be modelled for *human* NHE1 in complex with Calcineurin B homologous protein 1 (CHP1)(Dong *et al.*, 2021). Structures of human NHE1-CHP1 in outward and inward-facing states show some differences in the position of the C-terminal tail (Dong *et al.*, 2021). Based on these structural differences, it was proposed that CHP1 may increase activity by favouring an outward-facing state. In the improved the NHE9*CC structure we could model the corresponding region of the C-terminal tail, but in the absence of any interacting regulatory proteins. Surprisingly, we find that NHE9*CC has a similar interfacial helix between the core and dimer domains to that seen in NHE1. However, in the absence of a regulatory protein, the C-terminal interfacial helix in NHE9*CC is making a number of direct contacts with the linker helix TM7, likely restricting its mobility and that of the core transport domains. An autoinhibitory role of the C-terminal tail has been previously proposed for NHE1 (Wakabayashi *et al.*, 1997), which is removed upon $Ca^{2+}$-calmodulin binding to a site distal to the peripheral helix (Sjogaard-Frich *et al*, 2021). Our structure of NHE9*CC implies that the C-terminal tail may act in an autoinhibitory manner in all the NHEs in the absence of binding partners. It, thus, seems likely that the relocation of an auto-inhibitory C-terminal tail by binding partners could represent a general mode for positive allosteric regulation in all NHEs. Nevertheless, it's possible positive regulators like $Ca^{2+}$-calmodulin, can both displace this C-terminal helix and promote homodimerization by itself forming oligomers (Sjogaard-Frich *et al.*, 2021). Furthermore, $PIP_2$ lipids interacting with the C-terminal tail and its degree of phosphorylation may all contribute to the mobility of the CTD, and the ultimate level of autoinhibition apparent under resting conditions. Indeed, the complexity of auto-regulation was seen in a more recent structure of *human* NHE3, which was still in an auto-inhibited state with CHP1 bound, as distal loop downstream of the CTD helix was found to have protruded into the inward-facing cavity (Dong *et al*, 2022).

**Summary**

Our work provides a molecular framework for the allosteric regulation of NHE9 by modulating oligomerization in a specific lipid-dependent manner. The structure of the extracellular TM2-TM3 β-loop domain expands the possibilities for pharmacological

control of NHE9 and provides a conceptual framework for how the cell might control transporters by regulating their oligomerization with organelle-specific cues. Recently, it was shown that plant hormone (auxin) PIN-formed transporters are functional homodimers sharing the same fold as the $Na^+/H^+$ exchangers (Su *et al*, 2022; Ung *et al*, 2022; Yang *et al*, 2022). PIN transporters likewise harbour a C-terminal regulatory domain of varying length (Krecek *et al*, 2009), and also have both organellar and plasma membrane isoforms (Mravec *et al*, 2009), which must be regulated individually. Moreover, it has been shown that the plasma membrane localized PIN1 is in a dynamic equilibrium between monomers and dimers, and that the dimeric form can be regulated in the plant cell by endogenous flavonols (Teale *et al*, 2021). Thus, the allosteric regulatory mechanisms shown here could reveal themes relevant to other transporters in general.

## Materials and Methods

### Expression and purification of NHE9* and its variants

The *horse* NHE9* structural construct (UniProt accession: F7B133) was identified previously (Winklemann *et al.*, 2020), and is partially truncated on the C-terminal tail consisting of residues 8 to 575 out of a total of 644. The constructs NHE9*CC, NHE9*(N243A-D244A), NHE9*(K85Q-K105Q-K107Q) were synthesized and cloned into the GAL1 inducible TEV-site containing GFP-TwinStrep-$His_8$ vector $pDDGFP_3$. The cloned *horse* NHE9* and its variants were transformed into the *S. cerevisiae* strain FGY217 and cultivated in 24-L cultures of minus URA media with 0.2% of glucose at 30°C at 150 RPM Tuner shaker flasks using Innova 44R incubators (New Brunswick). Upon reaching an $OD_{600}$ of 0.6 AU galactose was added to a final concentration of 2% (w/v) to induce protein overexpression. Following incubation at the same conditions the cells were harvested 22h after induction by centrifugation (5,000 × *g*, 4°C, 10 min). The cells were resuspended in cell resuspension buffer (CRB, 50 mM Tris-HCl pH 7.6, 1 mM EDTA, 0.6 M sorbitol) and subsequently lysed by mechanical disruption as previously described(Drew *et al*, 2008). Centrifugation (10,000 × *g*, 4°C, 10 min) was used to remove cell debris. Membranes were subsequently isolated from the supernatant by ultracentrifugation (195,000 × *g*, 4°C, 2 h), resuspended and homogenized in

membrane resuspension buffer (MRB 20 mM Tris-HCl pH 7.5, 0.3 M sucrose, 0.1 mM $CaCl_2$).

For structural studies of NHE9* at pH 6.5, the membranes were extracted and purified as described previously (Winklemann *et al.*, 2020). In short, the Streptag-purified protein after removal of the C-terminal affinity-GFP-tag was collected and concentrated using 100 kDa MW cut-off spin concentrator (Amicon Merck-Millipore) further purified by size-exclusion chromatography (SEC), using a Superose 6 increase 10/300 column (GE Healthcare) and an Agilent LC-1220 system in 20 mM Mes-Tris pH 6.5, 150 mM NaCl, 0.003% (w/v) LMNG, 0.0006% (w/v) CHS. For NHE9*CC, the isolated membranes were solubilized as mentioned before (Winklemann *et al.*, 2020) with addition of brain extract from bovine brain type VII (Sigma-Aldrich, cat. nr. B3635) to a total concentration of 0.003mg/ml, in the solublization, wash and elution buffers (Winklemann *et al.*, 2020). The cleaved protein was collected and concentrated using 100 kDa MW cut-off spin concentrators (Amicon Merck-Millipore) separated by size-exclusion chromatography (SEC), using a Superose 6 increase 10/300 column (GE Healthcare) and an Agilent LC-1220 system in 20 mM Tris-HCl pH 7.5, 150 mM NaCl, 0.003% (w/v) LMNG, 0.0006% (w/v) CHS.

*Expression and purification of EcNhaA-mut2*

*Ec*NhaA WT-like triple mutant (A109T, Q277G, L296M), with a TEV-cleavable C-terminal GFP-$His_8$ tag was overexpressed in the *E. coli* strain Lemo21 (DE3) and purified as previously described (Lee *et al.*, 2014). Briefly, the *Ec*NhaA triple mutant was extracted from membranes with *n*-Dodecyl β-D-maltoside (DDM; Glycon) and purified by Ni-nitrilotriacetic acid (Ni-NTA; Qiagen) affinity chromatography. To purified NhaA-triple-mutant-GFP fusion, a final concentration of 3 mM cardiolipin (18:1) in 0.05% DDM was added, and then dialyzed overnight against buffer consisting of 20 mM Tris-HCl pH 7.5, 150 mM NaCl and 0.03% DDM. The dialysed NhaA-triple-mutant-GFP fusion was subjected to size-exclusion chromatography and the peak concentrated to 3.5 $mg.ml^{-1}$.

**Cryo-EM sample preparation and data acquisition and processing**

3 µg of purified NHE9*CC sample was applied to freshly glow-discharged Quantifoil R2/1 Cu300 mesh grids (Electron Microscopy Sciences) and blotted for 3.0s with a 20s waiting time prior, under 100% humidity and subsequently plunge frozen in liquid ethane using a Vitrobot Mark IV (Thermo Fisher Scientific). Cryo-EM datasets were collected on a Titan Krios G3i electron microscope operated at 300 kV equipped with a GIF (Gatan) and a K3 Bioquantum direct electron detector (Gatan) in counting mode. The movie stacks were collected at 130,000× magnification corresponding to a pixel size of 0.66 Å in a counted super-resolution mode. All movies were recorded with a defocus range of -0.4 to -2.5 µm. Similarly, 2.4 µg of purified NHE9* at pH 6.5 was blotted and the movie stacks were collected at 165,000x magnification, with a pixel size of 0.82 Å on Titan Krios G2 electron microscope operated at 300 kV equipped with a GIF (Gatan) and a K2 summit direct electron detector (Gatan) in counting mode The movies were recorded with a defocus range of -0.9 to -2.3 µm. 3µl of *Ec*NhaA-mut2 with concentration of 3.5mg/ml was blotted and the movie stack was collected at 130,000x magnification, with a pixel size of 0.6645 Å. The movies were recorded with a defocus range of -0.6 to -2.0 µm. The statistics of all cryo-EM data acquisition are summarized in Supplementary Table 1.

*Image processing NHE9* at pH 6.5:*

The dose-fractioned movies were corrected by using MotionCorr2 (Zheng *et al*, 2017). The dose-weighted micrographs were used for contrast-transfer-function estimation by CTFFIND-4.1.13 (Rohou & Grigorieff, 2015). The dose-weighted images were used for auto-picking, classification and 3D reconstruction. Approximately 1,000 particles were manually picked, followed by a round of 2D classification to generate templates for a subsequent round of auto-picking using RELION-3.0 beta (Zivanov *et al*, 2018). The auto-picked particles were subjected to multiple rounds of 2D classification using RELION-3.0 beta to remove bad particles and "junk". The particles belonging to "good" 2D classes were extracted and used for initial model generation using RELION-3.0 beta (Zivanov *et al.*, 2018).

To visualize the extracellular loop domain of NHE9, the aligned 244,279 particles from RELION was imported into CryoSPARC (Punjani *et al.*, 2017). *UCSF pyem (Daniel*

*Asarnow, 2019)* was used for file format conversion from RELION to CryoSPARC. 3D Variability Analysis (3DVA) in CryoSPARC (Punjani *et al.*, 2017) was performed and set up 6 variable components with the filter resolution 4 Å and high-pass filter 20 Å, respectively. After cluster analysis, the remaining 103,815 particles in 1 of 3 cluster was selected and subsequently, homogeneous refinement in CryoSPARC was performed after applying C2 symmetry and the reconstructed map reached to 3.1 Å resoltuion at the gold standard FSC (0.143).

*Image processing NHE9*CC:*

The dataset was processed using CryoSPARC (Punjani *et al.*, 2017). Dose fractionated movie frames were aligned using "patch motion correction," and contrast transfer function (CTF) were estimated using "Patch CTF estimation". The particles were picked using automated blob picker. Particles with good 2D classes were used for template based particle picking and extracted using a box size of 300 pixels. 268,054 particles were further used for *ab initio* model building and hetero refinements. Final round of non-uniform refinement with C2 symmetry and masked local refinement did result in 3D reconstruction with a gold standard FSC resolution estimation of 3.15Å.

*Image processing EcNhaA-mut2:*

14,329 dose fractionated movie frames were aligned using "patch motion correction," and contrast transfer function (CTF) were estimated using "Patch CTF estimation" in CryoSPARC (Punjani *et al.*, 2017). 4,401,429 particles were extracted and cleaned up using multiple rounds of 2D classification. 542,404 particles were used for *ab initio* model building and cleaned using multiple rounds of hetero refinement. 78,917 particles were further selected for a final round of non-uniform refinement and masked local refinement which resulted in 3D reconstruction with a gold standard FSC resolution estimation of 3.37Å.

**Cryo EM model building and refinement**

Previously determined NHE9 structure (PDB id: 6Z3Z) was fitted into the cryoEM density map of NHE9* CC mutant. Iterative model building and real space refinement was performed using COOT (Emsley *et al*, 2010) and PHENIX.refine (Afonine *et al*, 2018). Prior to model building of the extracellular loop domain, AlphaFold2 (AF2) with poly-glycine linker was performed to predict the NHE9 dimer structure assembly. After

automatically fitting the initial model into the cryo-EM map, iterative model building and real space refinement was performed using COOT (Emsley *et al.*, 2010) and PHENIX.refine (Afonine *et al.*, 2018). The refinement statistics are summarized in Supplementary Table 1. For generating structural figures PyMOL was used, and for figures of cryo-EM maps either Chimera (Pettersen *et al*, 2004) or ChimeraX (Pettersen *et al*, 2021) was used.

**GFP-based thermal shift assay**

To characterize lipid binding for NHE9* we used the GFP-Thermal Shift assay (Chatzikyriakidou *et al*, 2021). In brief, purified NHE9*-GFP fusions was isolated as described previously (Winklemann *et al.*, 2020). A buffer containing 20mM Tris, 150mM NaCl and 0.03% (w/v) DDM 0.006% (w/v) CHS was used to dilute samples to a final concentration of 0.05–0.075 mg/ml with DDM added to a final concentration of 1% (w/v), and incubated for 30 min at 4°C. Stock solutions of the respective lipids, phosphatidylinositol-bis-4,5-phosphate (PI-(4,5)$P_2$ dioctanoyl Echelon Biosciences cat no. P-4508), and phosphatidylinositol-bis-3,5-phosphate (PI-(3,5)$P_2$ dipalmitoyl, Echelon Biosciences cat no. P-3516) were prepared with final concentration of 1 mg/ml in buffer mentioned above. Respective lipids were added to purified NHE9* sample to a final concentration of 0.1 mg/ml and incubated for 10 mins on ice. Subsequently, β-D-Octyl glucoside (Anatrace) was added to a final concentration of 1% (w/v) in 300 µl and the sample aliquots of 100 µl were heated at individual temperatures ranging from 20-80°C for 10 min using a PCR thermocycler (Veriti, Applied Biosystems). Heat-denatured material was pelleted at 5000 × g for 30 min at 4°C. The resulting supernatants were collected and fluorescence values recorded (Excitation: 488, Emission 512 nm) using 96-well plate (Thermo Fisher Scientific) measured with Fluoroskan microplate fluorometer (Thermo Scientific) reader. The apparent *T*m was calculated by plotting the average GFP fluorescence intensity from three technical repeats per temperature and fitting a resulting curve using a sigmoidal 4-parameter logistic regression using GraphPad Prism software (GraphPad Software Inc.). The $\Delta T_M$ was calculated by subtracting the apparent $T_M$ of the lipid free sample, from the apparent $T_M$ of the sample with the respective lipid added.

**Solid Supported Membrane-based electrophysiology**

For SSM-based electrophysiology measurements, protein was reconstituted in yeast polar lipids (Avanti). The lipids were prepared by solubilization in chloroform and dried using a rotary evaporator (Hei-Vap Core, Heidolph Instruments). Dry lipids were thoroughly resuspended in 10 mM MES-Tris pH 8.5, 10 mM $MgCl_2$ buffer at a final concentration of 10 mg $ml^{-1}$. Unilamellar vesicles were prepared by extruding the resuspended lipids using an extruder (Avestin) with 400-nm polycarbonate filters (Whatman). The vesicles were destabilized by the addition of Na-cholate (0.65% w/v final concentration). SEC-purified protein was added to the destabilized liposomes at a lipid-to-protein ratio (LPR) of 5:1 and incubated for 5 min at room temperature. The sample was added to a PD SpinTrap G-25 desalting column for removing detergent and the reconstituted proteoliposomes were collected in a final volume of 100µl. The sample was diluted to final lipid concentration of 5 mg $ml^{-1}$ in 10mM MES-Tris pH 7.5, 10 mM $MgCl_2$ buffer, flash frozen I liquid nitrogen and stored at −80 °C. Proteoliposomes were diluted 1:1 (vol/vol) with non-activating buffer (10 mM MES-Tris pH 7.5, 300 mM Choline chloride, 10 mM $MgCl_2$) and sonicated using a bath sonicator. 10µl of sample was loaded on 1mm sensor. For sample measured with lipid PI-(3,5)$P_2$, 20µM of lipid was added to the protein and incubated for 15 min. The sample was again reconstituted in yeast polar lipids for making proteoliposomes using the protocol mentioned above.

Sensor preparation for SSM-based electrophysiology using the SURFE$^2$R N1(Nanion Technologies) system was performed as described previously (Bazzone *et al.*, 2017). During the experiments, NHE9 was activated by solution exchange from non-activating buffer to an activating buffer containing the substrate i.e NaCl. For binding kinetics measurements, *x* mM Choline chloride was replaced by (300-x) mM NaCl in the activating buffer to get peaks corresponding to increase in substrate concentration. For kinetic analysis, the response to increasing concentrations of NaCl was fitted from triplicate measurements to nonlinear regression curve-fit to one site specific binding using GraphPad Prism software. The peak current values were normalized with respect to the average of maximum value obtained for all measurements. The final $K_d$ values reported are the mean ± s.d. of n = 3 independent sensors.

**All-atom molecular dynamics simulations**

The NHE9* CC structure and NHE9* TM2-TM3 loop variant (K58Q, K105Q, K107Q) were embedded into the POPC bilayer and solvated in 0.15 M NaCl using CHARMM-GUI (Qi *et al*, 2015). Either PI-(3,5)$P_2$ and PI-(4,5)$P_2$ were placed in the $PIP_2$ binding site identified from the cryo-EM structure. All simulations were simulated with a 2 fs timestep using the CHARMM36m forcefield in GROMACS 2022.1(Abraham, 2015). The system was then energy minimised and equilibrated using the standard CHARMM-GUI protocol (Abraham, 2015), where the last step of the protocol was extended to 5 ns. The production runs were conducted for 250 ns under 303.15 K using the v-rescale thermostat. The pressure of all systems was maintained at 1 bar using a C-rescale barostat. All simulations were carried out in triplicates, where simulation frames were saved every 0.1 ns.

## References

The PyMOL Molecular Graphics System, Version 1.2r3pre ed. Schrödinger, LLC.

Abraham MM, T; Roland, S; Páll, S; Smith, J; Hess, B;Lindahl, E (2015) GROMACS: High performance molecular simulations through multi-level parallelism from laptops to supercomputers. *SoftwareX* 1: 19-25

Afonine PV, Poon BK, Read RJ, Sobolev OV, Terwilliger TC, Urzhumtsev A, Adams PD (2018) Real-space refinement in PHENIX for cryo-EM and crystallography. *Acta Crystallogr D Struct Biol* 74: 531-544

Aharonovitz O, Zaun HC, Balla T, York JD, Orlowski J, Grinstein S (2000) Intracellular pH regulation by Na(+)/H(+) exchange requires phosphatidylinositol 4,5-bisphosphate. *J Cell Biol* 150: 213-224

Alhadeff R, Warshel A (2015) Simulating the function of sodium/proton antiporters. *Proc Natl Acad Sci U S A* 112: 12378-12383

Arkin IT, Xu H, Jensen MO, Arbely E, Bennett ER, Bowers KJ, Chow E, Dror RO, Eastwood MP, Flitman-Tene R *et al* (2007) Mechanism of Na+/H+ antiporting. *Science* 317: 799-803

Bazzone A, Barthmes M, Fendler K (2017) SSM-Based Electrophysiology for Transporter Research. *Methods in enzymology* 594: 31-83

Brett CL, Donowitz M, Rao R (2005) Evolutionary origins of eukaryotic sodium/proton exchangers. *Am J Physiol Cell Physiol* 288: C223-239

Chatzikyriakidou Y, Ahn DH, Nji E, Drew D (2021) The GFP thermal shift assay for screening ligand and lipid interactions to solute carrier transporters. *Nat Protoc* 16: 5357-5376

762 Coincon M, Uzdavinys P, Nji E, Dotson DL, Winkelmann I, Abdul-Hussein S, Cameron
763 AD, Beckstein O, Drew D (2016) Crystal structures reveal the molecular basis of ion
764 translocation in sodium/proton antiporters. *Nat Struct Mol Biol* 23: 248-255
765 Corey RA, Song W, Duncan AL, Ansell TB, Sansom MSP, Stansfeld PJ (2021)
766 Identification and assessment of cardiolipin interactions with E. coli inner membrane
767 proteins. *Sci Adv* 7
768 Daniel Asarnow EP, & Yifan Cheng. , 2019. UCSF pyem v0.5. Zenodo. p.
769 http://doi.org/10.5281/zenodo.3576630.
770 de Lartigue J, Polson H, Feldman M, Shokat K, Tooze SA, Urbe S, Clague MJ (2009)
771 PIKfyve regulation of endosome-linked pathways. *Traffic* 10: 883-893
772 Dong Y, Gao Y, Ilie A, Kim D, Boucher A, Li B, Zhang XC, Orlowski J, Zhao Y (2021)
773 Structure and mechanism of the human NHE1-CHP1 complex. *Nat Commun* 12: 3474
774 Dong Y, Li H, Ilie A, Gao Y, Boucher A, Zhang XC, Orlowski J, Zhao Y (2022)
775 Structural basis of autoinhibition of the human NHE3-CHP1 complex. *Sci Adv* 8:
776 eabn3925
777 Donowitz M, Ming Tse C, Fuster D (2013) SLC9/NHE gene family, a plasma
778 membrane and organellar family of Na(+)/H(+) exchangers. *Mol Aspects Med* 34: 236-
779 251
780 Donowitz M, Mohan S, Zhu CX, Chen TE, Lin R, Cha B, Zachos NC, Murtazina R,
781 Sarker R, Li X (2009) NHE3 regulatory complexes. *J Exp Biol* 212: 1638-1646
782 Dove SK, Cooke FT, Douglas MR, Sayers LG, Parker PJ, Michell RH (1997) Osmotic
783 stress activates phosphatidylinositol-3,5-bisphosphate synthesis. *Nature* 390: 187-192
784 Drew D, Boudker O (2016) Shared Molecular Mechanisms of Membrane Transporters.
785 *Annu Rev Biochem* 85: 543-572

786 Drew D, Newstead S, Sonoda Y, Kim H, von Heijne G, Iwata S (2008) GFP-based
787 optimization scheme for the overexpression and purification of eukaryotic membrane
788 proteins in Saccharomyces cerevisiae. *Nat Protoc* 3: 784-798
789 Emsley P, Lohkamp B, Scott WG, Cowtan K (2010) Features and development of Coot.
790 *Acta Crystallogr D Biol Crystallogr* 66: 486-501
791 Fliegel L (2019) Structural and Functional Changes in the Na(+)/H(+) Exchanger
792 Isoform 1, Induced by Erk1/2 Phosphorylation. *Int J Mol Sci* 20
793 Fuster DG, Alexander RT (2014) Traditional and emerging roles for the SLC9 Na+/H+
794 exchangers. *Pflugers Archiv : European journal of physiology* 466: 61-76
795 Gupta K, Donlan JAC, Hopper JTS, Uzdavinys P, Landreh M, Struwe WB, Drew D,
796 Baldwin AJ, Stansfeld PJ, Robinson CV (2017) The role of interfacial lipids in
797 stabilizing membrane protein oligomers. *Nature* 541: 421-424
798 Hasegawa J, Strunk BS, Weisman LS (2017) PI5P and PI(3,5)P2: Minor, but Essential
799 Phosphoinositides. *Cell Struct Funct* 42: 49-60
800 Hendus-Altenburger R, Kragelund BB, Pedersen SF (2014) Structural dynamics and
801 regulation of the mammalian SLC9A family of Na(+)/H(+) exchangers. *Curr Top*
802 *Membr* 73: 69-148
803 Ho CY, Alghamdi TA, Botelho RJ (2012) Phosphatidylinositol-3,5-bisphosphate: no
804 longer the poor PIP2. *Traffic* 13: 1-8
805 Huang Y, Chen W, Dotson DL, Beckstein O, Shen J (2016) Mechanism of pH-
806 dependent activation of the sodium-proton antiporter NhaA. *Nat Commun* 7: 12940
807 Hunte C, Screpanti E, Venturi M, Rimon A, Padan E, Michel H (2005) Structure of a
808 Na+/H+ antiporter and insights into mechanism of action and regulation by pH. *Nature*
809 435: 1197-1202

Jumper J, Evans R, Pritzel A, Green T, Figurnov M, Ronneberger O, Tunyasuvunakool K, Bates R, Zidek A, Potapenko A *et al* (2021) Highly accurate protein structure prediction with AlphaFold. *Nature* 596: 583-589

Kondapalli KC, Hack A, Schushan M, Landau M, Ben-Tal N, Rao R (2013) Functional evaluation of autism-associated mutations in NHE9. *Nat Commun* 4: 2510

Kondapalli KC, Llongueras JP, Capilla-Gonzalez V, Prasad H, Hack A, Smith C, Guerrero-Cazares H, Quinones-Hinojosa A, Rao R (2015) A leak pathway for luminal protons in endosomes drives oncogenic signalling in glioblastoma. *Nat Commun* 6: 6289

Kondapalli KC, Prasad H, Rao R (2014) An inside job: how endosomal Na(+)/H(+) exchangers link to autism and neurological disease. *Front Cell Neurosci* 8: 172

Kozachkov L, Padan E (2013) Conformational changes in NhaA Na+/H+ antiporter. *Mol Membr Biol* 30: 90-100

Krecek P, Skupa P, Libus J, Naramoto S, Tejos R, Friml J, Zazimalova E (2009) The PIN-FORMED (PIN) protein family of auxin transporters. *Genome Biol* 10: 249

Lacroix J, Poet M, Maehrel C, Counillon L (2004) A mechanism for the activation of the Na/H exchanger NHE-1 by cytoplasmic acidification and mitogens. *EMBO Rep* 5: 91-96

Landreh M, Marklund EG, Uzdavinys P, Degiacomi MT, Coincon M, Gault J, Gupta K, Liko I, Benesch JL, Drew D *et al* (2017) Integrating mass spectrometry with MD simulations reveals the role of lipids in Na(+)/H(+) antiporters. *Nature communications* 8: 13993

Lee C, Kang HJ, von Ballmoos C, Newstead S, Uzdavinys P, Dotson DL, Iwata S, Beckstein O, Cameron AD, Drew D (2013) A two-domain elevator mechanism for sodium/proton antiport. *Nature* 501: 573-577

835 Lee C, Yashiro S, Dotson DL, Uzdavinys P, Iwata S, Sansom MS, von Ballmoos C,
836 Beckstein O, Drew D, Cameron AD (2014) Crystal structure of the sodium-proton
837 antiporter NhaA dimer and new mechanistic insights. *The Journal of general*
838 *physiology* 144: 529-544
839 Li SC, Diakov TT, Xu T, Tarsio M, Zhu W, Couoh-Cardel S, Weisman LS, Kane PM
840 (2014) The signaling lipid PI(3,5)P(2) stabilizes V(1)-V(o) sector interactions and
841 activates the V-ATPase. *Mol Biol Cell* 25: 1251-1262
842 Lin PJ, Williams WP, Luu Y, Molday RS, Orlowski J, Numata M (2005) Secretory
843 carrier membrane proteins interact and regulate trafficking of the organellar
844 (Na+,K+)/H+ exchanger NHE7. *J Cell Sci* 118: 1885-1897
845 Masrati G, Dwivedi M, Rimon A, Gluck-Margolin Y, Kessel A, Ashkenazy H, Mayrose
846 I, Padan E, Ben-Tal N (2018) Broad phylogenetic analysis of cation/proton antiporters
847 reveals transport determinants. *Nat Commun* 9: 4205
848 Matsuoka R, Fudim R, Jung S, Zhang C, Bazzone A, Chatzikyriakidou Y, Robinson
849 CV, Nomura N, Iwata S, Landreh M *et al* (2022) Structure, mechanism and lipid-
850 mediated remodeling of the mammalian Na(+)/H(+) exchanger NHA2. *Nat Struct Mol*
851 *Biol* 29: 108-120
852 Milosavljevic N, Monet M, Lena I, Brau F, Lacas-Gervais S, Feliciangeli S, Counillon
853 L, Poet M (2014) The intracellular Na(+)/H(+) exchanger NHE7 effects a Na(+)-
854 coupled, but not K(+)-coupled proton-loading mechanism in endocytosis. *Cell reports*
855 7: 689-696
856 Mravec J, Skupa P, Bailly A, Hoyerova K, Krecek P, Bielach A, Petrasek J, Zhang J,
857 Gaykova V, Stierhof YD *et al* (2009) Subcellular homeostasis of phytohormone auxin
858 is mediated by the ER-localized PIN5 transporter. *Nature* 459: 1136-1140

Nakamura N, Tanaka S, Teko Y, Mitsui K, Kanazawa H (2005) Four Na+/H+ exchanger isoforms are distributed to Golgi and post-Golgi compartments and are involved in organelle pH regulation. *J Biol Chem* 280: 1561-1572

Nji E, Chatzikyriakidou Y, Landreh M, Drew D (2018) An engineered thermal-shift screen reveals specific lipid preferences of eukaryotic and prokaryotic membrane proteins. *Nature communications* 9: 4253

Norholm AB, Hendus-Altenburger R, Bjerre G, Kjaergaard M, Pedersen SF, Kragelund BB (2011) The intracellular distal tail of the Na+/H+ exchanger NHE1 is intrinsically disordered: implications for NHE1 trafficking. *Biochemistry* 50: 3469-3480

Odunewu-Aderibigbe A, Fliegel L (2014) The Na(+) /H(+) exchanger and pH regulation in the heart. *IUBMB Life* 66: 679-685

Orlowski J, Grinstein S (2004) Diversity of the mammalian sodium/proton exchanger SLC9 gene family. *Pflugers Archiv : European journal of physiology* 447: 549-565

Padan E (2008) The enlightening encounter between structure and function in the NhaA Na+-H+ antiporter. *Trends Biochem Sci* 33: 435-443

Paulino C, Kuhlbrandt W (2014) pH- and sodium-induced changes in a sodium/proton antiporter. *Elife* 3: e01412

Paulino C, Wohlert D, Kapotova E, Yildiz O, Kuhlbrandt W (2014) Structure and transport mechanism of the sodium/proton antiporter MjNhaP1. *eLife* 3: e03583

Pedersen SF, Counillon L (2019) The SLC9A-C Mammalian Na(+)/H(+) Exchanger Family: Molecules, Mechanisms, and Physiology. *Physiol Rev* 99: 2015-2113

Pettersen EF, Goddard TD, Huang CC, Couch GS, Greenblatt DM, Meng EC, Ferrin TE (2004) UCSF Chimera--a visualization system for exploratory research and analysis. *J Comput Chem* 25: 1605-1612

Pettersen EF, Goddard TD, Huang CC, Meng EC, Couch GS, Croll TI, Morris JH, Ferrin TE (2021) UCSF ChimeraX: Structure visualization for researchers, educators, and developers. *Protein Sci* 30: 70-82

Prasad H (2021) Protons to Patients: targeting endosomal Na(+) /H(+) exchangers against COVID-19 and other viral diseases. *FEBS J* 288: 5071-5088

Punjani A, Rubinstein JL, Fleet DJ, Brubaker MA (2017) cryoSPARC: algorithms for rapid unsupervised cryo-EM structure determination. *Nat Methods* 14: 290-296

Qi Y, Ingolfsson HI, Cheng X, Lee J, Marrink SJ, Im W (2015) CHARMM-GUI Martini Maker for Coarse-Grained Simulations with the Martini Force Field. *J Chem Theory Comput* 11: 4486-4494

Quick M, Dwivedi M, Padan E (2021) Insight into the direct interaction of Na(+) with NhaA and mechanistic implications. *Sci Rep* 11: 7045

Rimon A, Mondal R, Friedler A, Padan E (2019) Cardiolipin is an Optimal Phospholipid for the Assembly, Stability, and Proper Functionality of the Dimeric Form of NhaA Na(+)/H(+) Antiporter. *Sci Rep* 9: 17662

Rohou A, Grigorieff N (2015) CTFFIND4: Fast and accurate defocus estimation from electron micrographs. *J Struct Biol* 192: 216-221

Romantsov T, Guan Z, Wood JM (2009) Cardiolipin and the osmotic stress responses of bacteria. *Biochim Biophys Acta* 1788: 2092-2100

Shimada-Shimizu N, Hisamitsu T, Nakamura TY, Hirayama N, Wakabayashi S (2014) Na+/H+ exchanger 1 is regulated via its lipid-interacting domain, which functions as a molecular switch: a pharmacological approach using indolocarbazole compounds. *Mol Pharmacol* 85: 18-28

Sjogaard-Frich LM, Prestel A, Pedersen ES, Severin M, Kristensen KK, Olsen JG, Kragelund BB, Pedersen SF (2021) Dynamic Na(+)/H(+) exchanger 1 (NHE1) -

908 calmodulin complexes of varying stoichiometry and structure regulate Ca(2+)-
909 dependent NHE1 activation. *Elife* 10
910 Slepkov ER, Rainey JK, Sykes BD, Fliegel L (2007) Structural and functional analysis
911 of the Na+/H+ exchanger. *Biochem J* 401: 623-633
912 Slonchak A, Clarke B, Mackenzie J, Amarilla AA, Setoh YX, Khromykh AA (2019)
913 West Nile virus infection and interferon alpha treatment alter the spectrum and the
914 levels of coding and noncoding host RNAs secreted in extracellular vesicles. *BMC*
915 *Genomics* 20: 474
916 Su N, Zhu A, Tao X, Ding ZJ, Chang S, Ye F, Zhang Y, Zhao C, Chen Q, Wang J *et al*
917 (2022) Structures and mechanisms of the Arabidopsis auxin transporter PIN3. *Nature*
918 Suades A, Qureshi A, McComas SE, Coincon M, Rudling A, Chatzikyriakidou Y,
919 Landreh M, Carlsson J, Drew D (2023) Establishing mammalian GLUT kinetics and
920 lipid composition influences in a reconstituted-liposome system. *Nat Commun* 14: 4070
921 Teale WD, Pasternak T, Dal Bosco C, Dovzhenko A, Kratzat K, Bildl W, Schworer M,
922 Falk T, Ruperti B, Schaefer JV *et al* (2021) Flavonol-mediated stabilization of PIN
923 efflux complexes regulates polar auxin transport. *The EMBO journal* 40: e104416
924 Ung KL, Winkler M, Schulz L, Kolb M, Janacek DP, Dedic E, Stokes DL, Hammes
925 UZ, Pedersen BP (2022) Structures and mechanism of the plant PIN-FORMED auxin
926 transporter. *Nature*
927 Wakabayashi S, Fafournoux P, Sardet C, Pouyssegur J (1992) The Na+/H+ antiporter
928 cytoplasmic domain mediates growth factor signals and controls "H(+)-sensing". *Proc*
929 *Natl Acad Sci U S A* 89: 2424-2428
930 Wakabayashi S, Ikeda T, Iwamoto T, Pouyssegur J, Shigekawa M (1997) Calmodulin-
931 binding autoinhibitory domain controls "pH-sensing" in the Na+/H+ exchanger NHE1
932 through sequence-specific interaction. *Biochemistry* 36: 12854-12861

933 Winkelmann I, Uzdavinys P, Kenney IM, Brock J, Meier PF, Wagner LM, Gabriel F,
934 Jung S, Matsuoka R, von Ballmoos C *et al* (2022) Crystal structure of the Na(+)/H(+)
935 antiporter NhaA at active pH reveals the mechanistic basis for pH sensing. *Nature*
936 *communications* 13: 6383
937 Winklemann I, Matsuoka R, Meier PF, Shutin D, Zhang C, Orellana L, Sexton R,
938 Landreh M, Robinson CV, Beckstein O *et al* (2020) Structure and elevator mechanism
939 of the mammalian sodium/proton exchanger NHE9. *EMBO J* 39: e105908
940 Wohlert D, Kuhlbrandt W, Yildiz O (2014) Structure and substrate ion binding in the
941 sodium/proton antiporter PaNhaP. *eLife* 3: e03579
942 Yang Z, Xia J, Hong J, Zhang C, Wei H, Ying W, Sun C, Sun L, Mao Y, Gao Y *et al*
943 (2022) Structural insights into auxin recognition and efflux by Arabidopsis PIN1.
944 *Nature*
945 Zhang-James Y, Vaudel M, Mjaavatten O, Berven FS, Haavik J, Faraone SV (2019)
946 Effect of disease-associated SLC9A9 mutations on protein-protein interaction
947 networks: implications for molecular mechanisms for ADHD and autism. *Atten Defic*
948 *Hyperact Disord* 11: 91-105
949 Zheng SQ, Palovcak E, Armache JP, Verba KA, Cheng Y, Agard DA (2017)
950 MotionCor2: anisotropic correction of beam-induced motion for improved cryo-
951 electron microscopy. *Nat Methods* 14: 331-332
952 Zivanov J, Nakane T, Forsberg BO, Kimanius D, Hagen WJ, Lindahl E, Scheres SH
953 (2018) New tools for automated high-resolution cryo-EM structure determination in
954 RELION-3. *eLife* 7

955

## Acknowledgements

We are grateful to Marta Carroni at the Cryo-EM Swedish National Facility at SciLife Stockholm for cryo-EM data collection as well as Michael Hall at the Umeå Core Facility for Electron Microscopy, UCEM and the European Synchrotron Radiation Facility (ESRF). The computations were enabled by resources provided by the Swedish National Infrastructure for Computing (SNIC) at the PDC Center for High Performance Computing, KTH Royal Institute of Technology, partially funded by the Swedish Research Council through grant agreement no. 2018-05973. This work was funded a European Research Council (ERC) Consolidator Grant EXCHANGE (Grant no. ERC-CoG-820187) to D.D

## Author contributions

D.D. designed the project. Cloning, expression screening and sample preparation for cryo-EM was carried out by P.M. and S.K. Cryo-EM data collection and map reconstruction was carried out by P.M, S.K, R.M, A.G an D.D. Model building was carried out by R.M, A.G and D.D. MD simulations were carried out by T.D and L.D. All authors discussed the results and commented on the manuscript. The authors declare no competing financial interests. Correspondence and request for materials should be addressed to D.D. (d.drew@dbb.su.se).

## Data availability

The coordinates and the maps for cryo-EM structures of *horse* NHE9* with TM2-TM3 loop at pH 6.5, *hor*se NHE9* CC bound to PI-(3,5)$P_2$, and the *E. coli* NhaA dimer with cardiolipin, have been deposited in the Protein Data Bank (PDB) and Electron Microscopy Data Bank (EMD) with entries PDB ID: 8PVR, 8PXB, 8PS0, respectively.

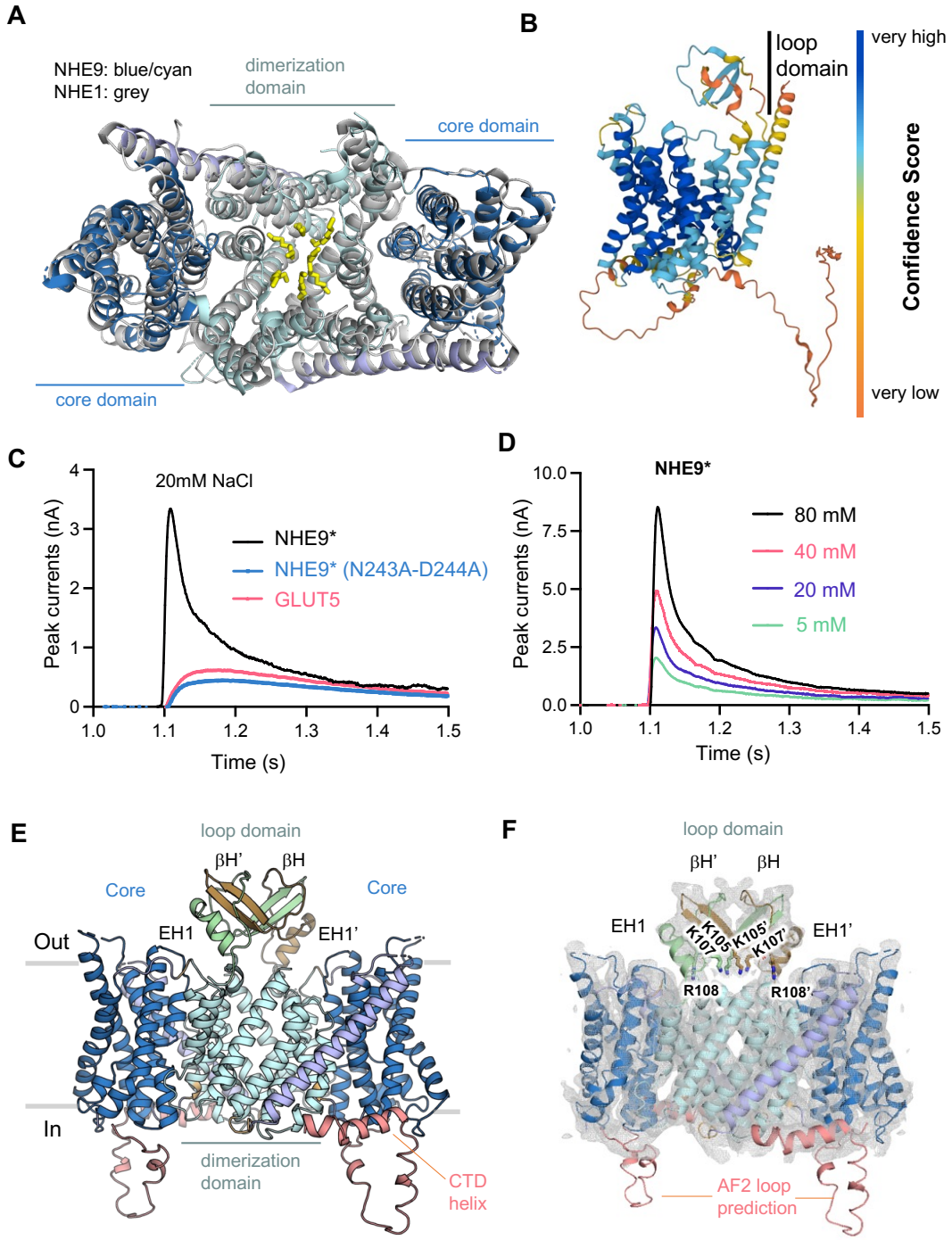


**Figure 1. SSM-based electrophysiology and cryo EM NHE9* structure with TM2-TM3 β-loop domain modelled**. (**A**) Structural superimposition of NHE9 with inward-facing NHE1 ($C_\alpha$ RMSD = 2.91 Å) shows the overall structural conservation. Inward-facing NHE9 ΔCTD (PDB: 6Z3Z) with dimerization domain (cyan), core domain (blue) and TM7 linking helix (light-purple) all shown as cartoon. Inward-facing NHE1 (PDB: 7DSW) (grey, cartoon) with its lipids (yellow, sticks) inside the cavity between the

dimerization domains. (**B**) AF2 model of the human NHE9 monomer that predicts an additional TM2-TM3 loop domain containing a β-hairpin with reasonable confidence. (**C**) SSM-based electrophysiology. Transient currents were recorded for NHE9* proteoliposomes (black trace) at symmetrical pH 7.5 after the addition of 20 mM NaCl. Peak currents for an ion-binding site NHE9* variant N243A-D244A (blue trace) and fructose transporter GLUT5 (Suades *et al*, 2023) (red trace) after the addition of 20 mM NaCl are also shown (**D**) SSM-based electrophysiology measurements of NHE9* proteoliposomes with transient currents recorded after $Na^+$ concentration jumps at pH 7.5 on both sides. (**E**) AF2 model of the *horse* NHE9 dimer with an TM2-TM3 loop domain containing an β-hairpin (βH1, βH1') and extracellular helix (EH1, EH1') from each of the two protomers coloured in brown and green, respectively. The core domain (dark-blue), dimerization domain (light-blue) and CTD domain (salmon) is further highlighted. (**F**) The AF2 dimer model for *horse* NHE9 after its refinement into cryo EM maps, as shown in E with charged residues in loop domain highlighted in sticks. An additional C-terminal helix in the CTD could be modelled (salmon, cartoon), but there is no density to support the 20 residue AF2 loop model that is located between the end of the core domain and the beginning of the interfacial helix**.**

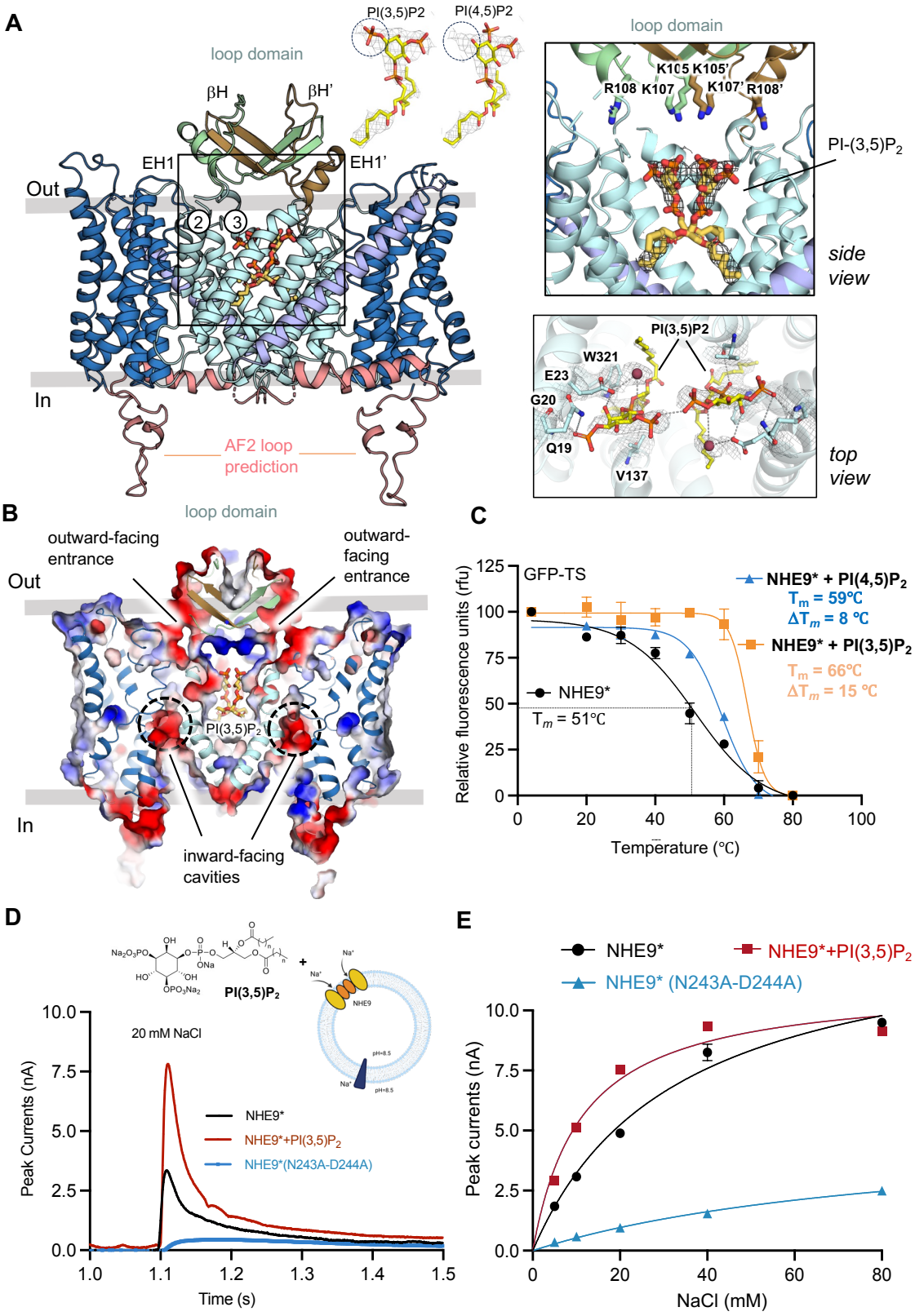


**Figure 2. TM2-TM3 β-loop domain structure of NHE9* CC with negatively-charged PI-(3,5)$P_2$ lipids bound at the dimer interface. (A)** *left:* Structure of the *horse* NHE9*CC determined by cryo-EM and guided by the refined NHE9* model for the β-hairpin TM2-TM3 loop domain. Domain-swapped βH, βH' and EH1, EH1' in

green and brown respectively, and NHE9 core and dimer domains coloured as in Fig. 1E. Two $PIP_2$ lipids (yellow sticks) are located in the middle at the dimerization interface between the two protomers and, in the insert above, the fitting of PI-(3,5)$P_2$ vs PI-(4,5)$P_2$ lipids into the cryo EM maps are compared. *right above:* Magnification of the two $PIP_2$ lipids, their interdomain binding groove and part of the loop-domain residues at the dimer interface. TM segments TM1 and TM8 are not shown for better visualization of the bound lipids. In total six positively-charged amino acids (K105, K107, R108 of each monomer) in the loop domains are positioned above the two negatively-charged PI-(3,5)$P_2$ lipids (yellow-sticks). *right below:* Inclusion of TM1 and TM8 helices and viewed from the extracellular side, shows the coordination of PI-(3,5)$P_2$ lipids (yellow sticks and grey mesh) by aromatic and polar residues **(B)** Electrostatic surface potential map cross-section with two negatively-charged PI-(3,5)$P_2$ modelled in the hydrophobic and positively-charged dimerization interface (blue). The interface between the loop domains and core domains (indicated by the black-line) are negatively-charged and provide an electrostatic pathway for cations in the outward-facing state. Protein shown as cartoon colored as in Fig. 1E, and PI-(3,5)$P_2$ as yellow-sticks and the ion-binding site is highlighted (dotted-circle). (**C**) Thermal shift stabilization of purified dimeric NHE9*-GFP in the presence of PI-(4,5)$P_2$ (blue) and PI-(3,5)$P_2$ (mustard) compared to lipid-free (black). Data presented are normalized fluorescence of mean values ± data range of n = 3 technical repeats; the apparent $T_M$ was calculated from datapoints fitted according to a sigmoidal 4-parameter logistic regression function. (**D**) *top*: Structure of the lipid PI(3,5)$P_2$ and its addition to NHE9 prior to incorporation into proteoliposomes and an illustration of the experimental setup. *Bottom:* resulting peak transient currents following addition of 20 mM NaCl under symmetrical pH conditions. (**E**) Fit of the amplitude of the transient currents as a function of $Na^+$ concentrations at pH 7.5 for horse NHE9* proteoliposomes pre-incubated with either buffer (black-trace) or synthetic PI-(3,5)$P_2$ lipids (red trace) and the corresponding binding affinity ($K_D$). Error bars are the mean values ± s.e.m. of: n = 3 individual repeats.

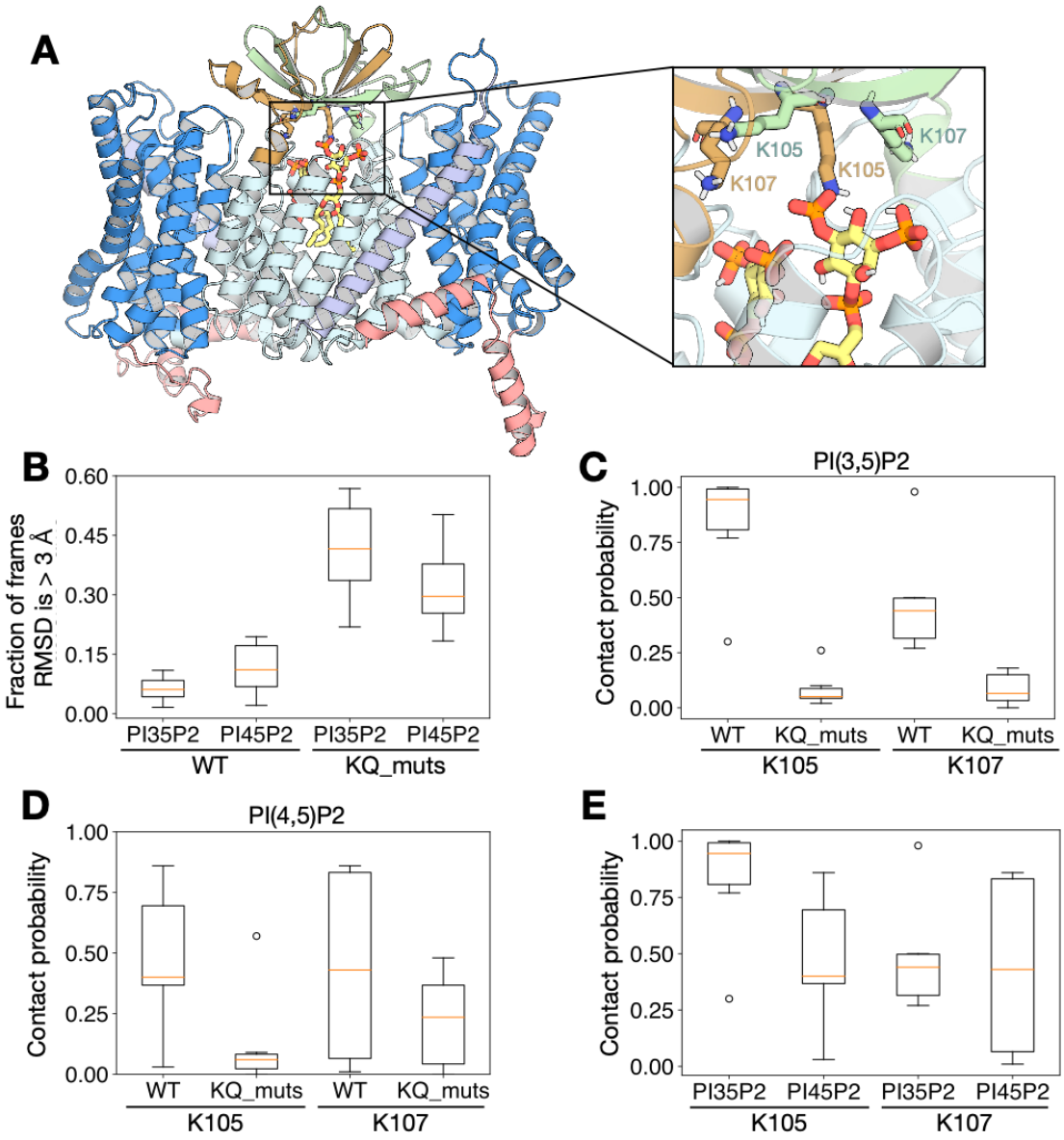


**Figure 3. MD simulations of $PIP_2$ interaction to NHE9* CC.** (**A**) A representative snapshot of NHE9 with PI-(3,5)$P_2$ after a 250 ns simulation. The structure of PI-(3,5)$P_2$ is shown in yellow. K105 and K107 on different chains are shown in green and brown, respectively. (**B**) Box plot representation of the distribution of the fractions of frames where the root mean square deviation (RMSD) of $PIP_2$ is > 3 Å with respect to its previous 10 ns structure. (**C**) Box plot representation of the distribution of frames where PI-(3,5)$P_2$ are within 4 Å (defined as contact probability) with either K105, K107 or its mutants. (**D**) Box plot representation of the distribution of frames where PI-(4,5)$P_2$ are within 4 Å (defined as contact probability) with either K105, K107 or its mutants. (**E**) Box plot representation of the distribution of the contact probability between K105 and K107 with either PI-(3,5)$P_2$ or PI-(4,5)$P_2$.

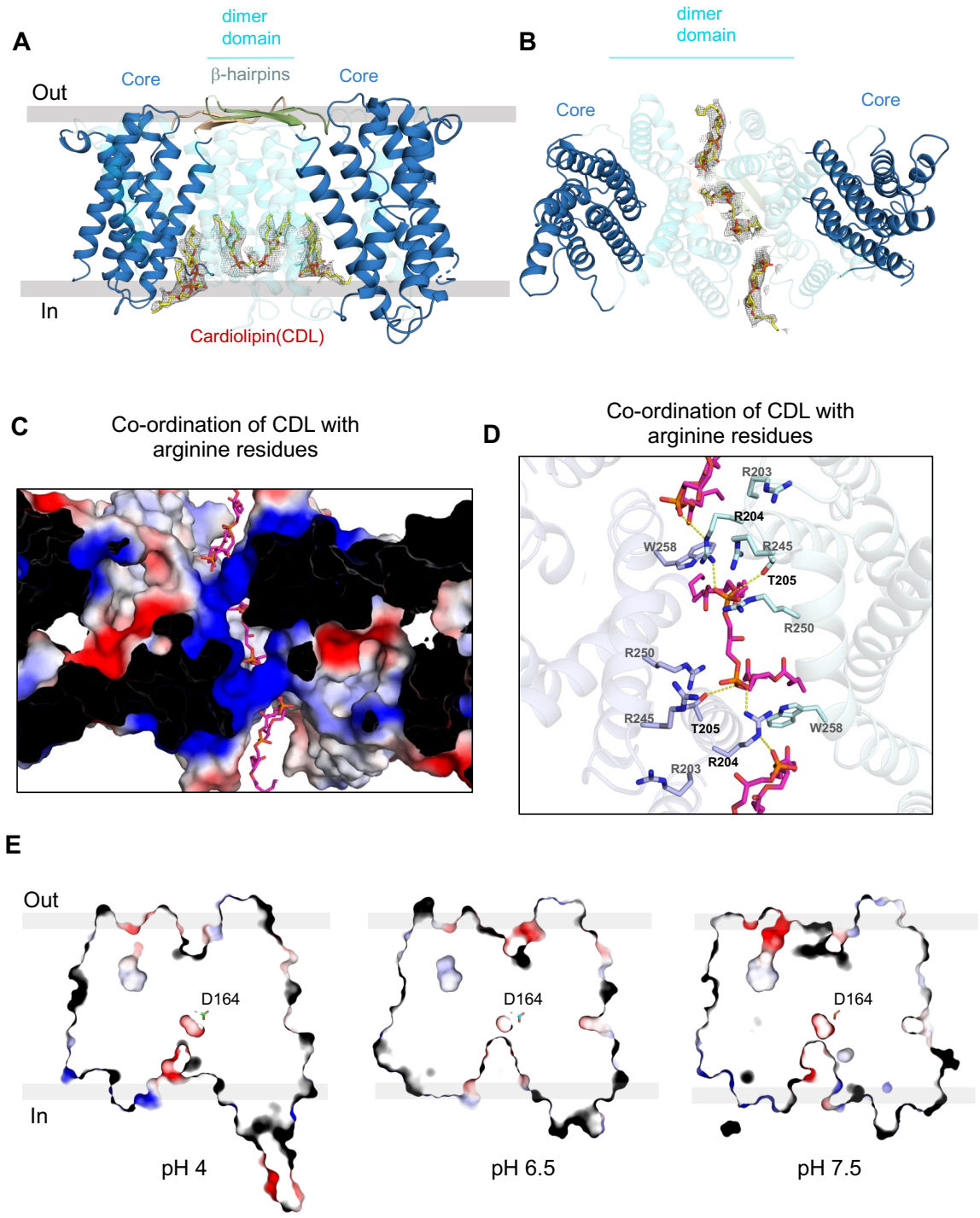


1053 **Figure 4. Structure of cardiolipin (CDL) bound to *Ec*NhaA homodimer.** (**A**) Model
1054 of *Ec*NhaA homodimer obtained by cryo-EM and with β-hairpin loop domains
1055 (palegreen, sand, cartoon). Large densities between the dimerization domains indicate
1056 the presence of three CDL (yellow, sticks) fitted in the model. (**B**) Cytoplasmic view of
1057 *Ec*NhaA model with the three CDL fitted between the dimer domains. (**C**) Cytoplasmic
1058 view of slice through an electrostatic surface potential map with three cardiolipins
1059 (mangenta, sticks) positioned in the hydrophobic and positively-charged dimerization

interface (blue). (**D**) Cytoplasmic view of *Ec*NhaA model (cartoon) with CDL (magenta, sticks) coordinating residues. Positively charged arginine residues are labelled and shown in cyan and purple sticks. (**E**) Slice through an electrostatic surface representation of *Ec*NhaA structures, perpendicular to the membrane plane, at active pH 6.5 (left, PDB ID: 7S24), inactive pH 4.0 (right, PDB ID: 4AU5) and pH 7.5-CDL bound. The ion-binding aspartate is indicated and shown as cyan sticks. The ion-binding funnel at the cytoplasmic side is much more open at active pH 6.5 and pH 7.5-CDL bound structure than at pH 4.

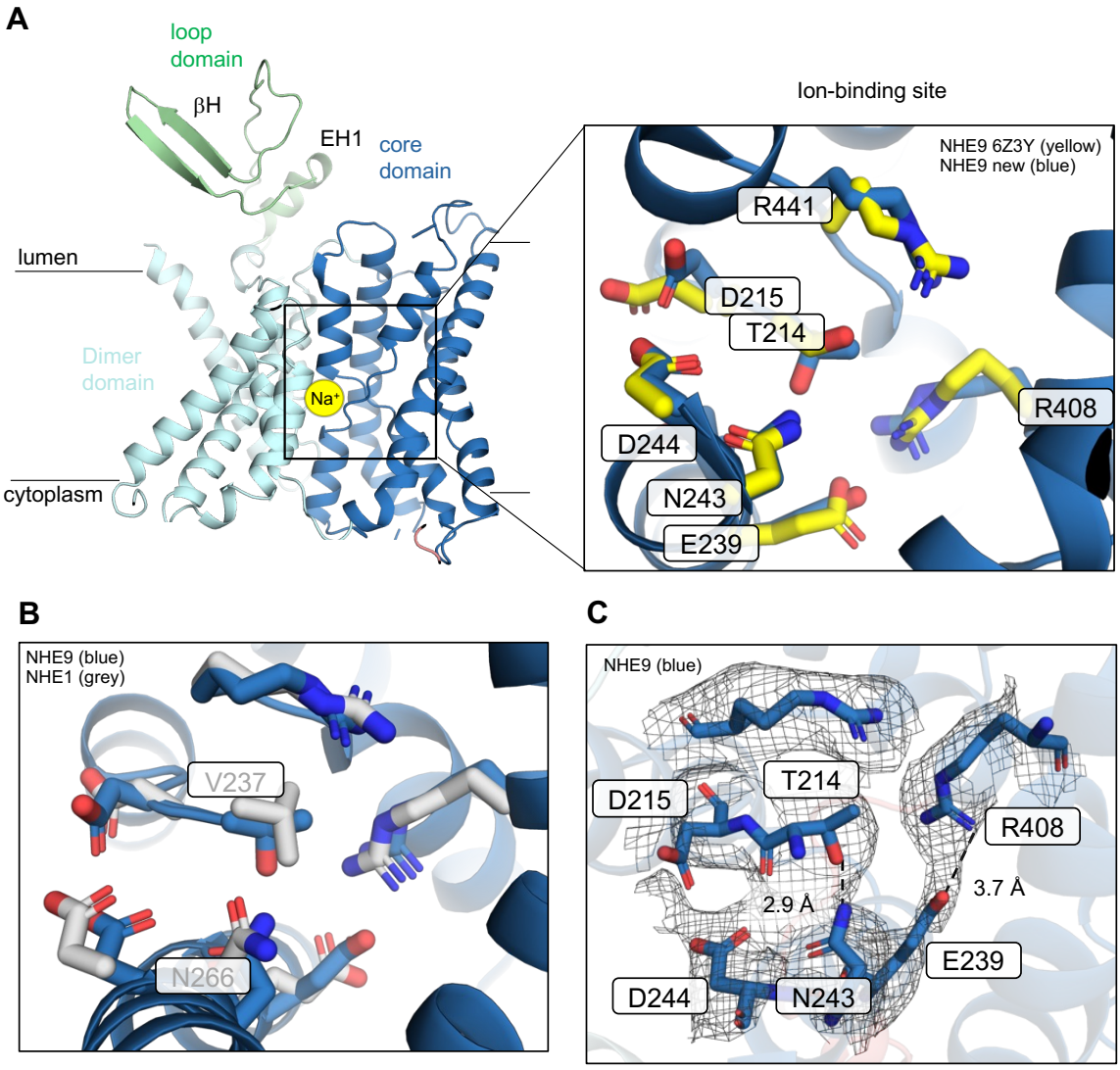


1080

1081 **Figure 5. Ion-binding site of the NHE9*CC (A)** *left:* cartoon representation of the
1082 NHE9 ion-binding site, located in the 6-TM core transporter domain, which is made up
1083 of two broken helices. The sodium ion (yellow sphere) is located and coordinated at the
1084 ion-binding site. *right:* ion-binding residues of the NHE9*CC structure are shown as
1085 blue sticks and labelled, with the identical residues of NHE9* shown as yellow sticks
1086 (PDB id: 6Z3Y). **(B)** Ion-binding residues of NHE9*CC are shown as blue sticks and
1087 NHE1 residues shown as grey sticks with Val237 labelled**. (C)** Hydrogen-bonding
1088 between T214-N243 and salt-bridge interaction between E239-R408 in the NHE9*CC
1089 structure are illustrated by dashed lines and the cryo EM maps shown as grey mesh..

1090

1091

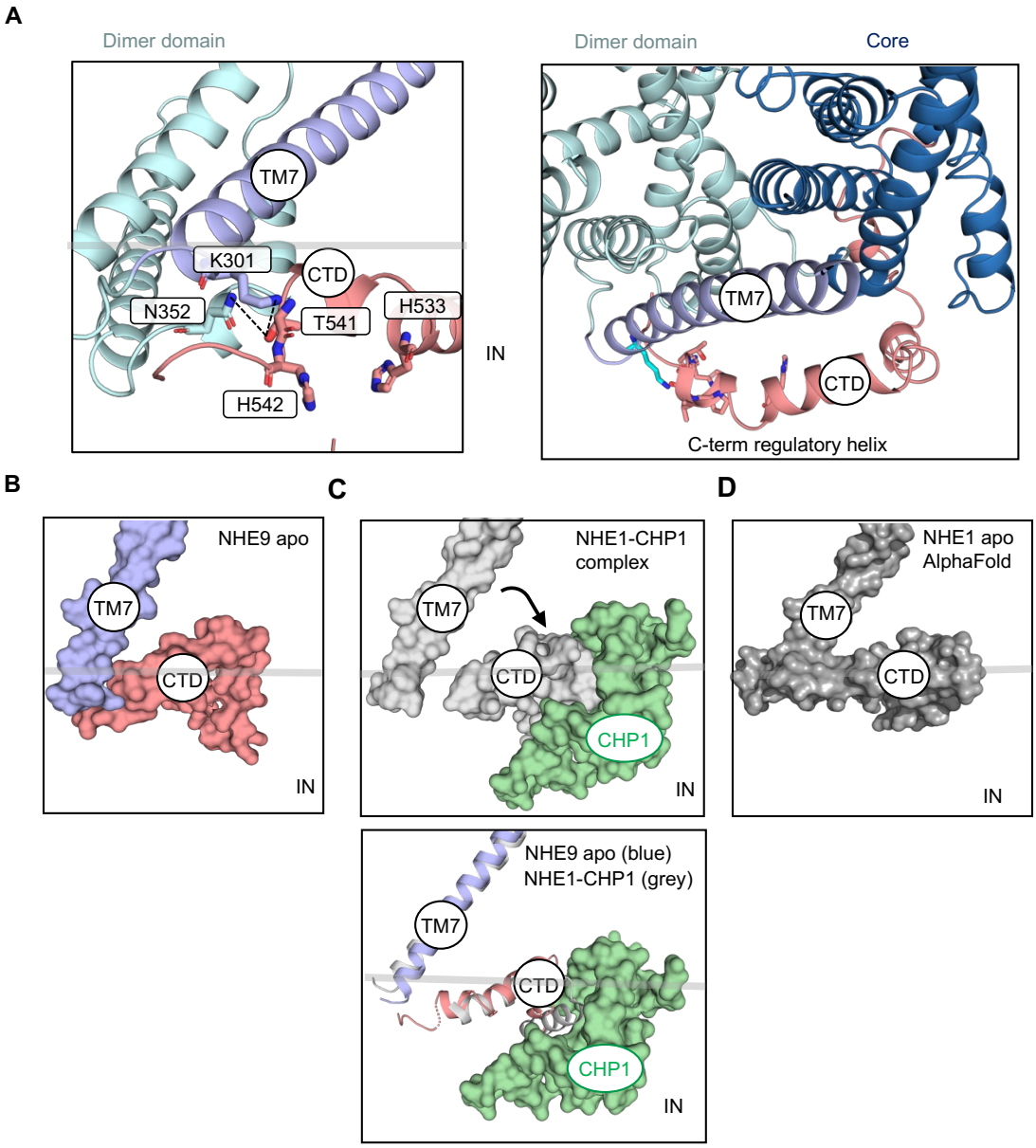


**Figure 6 The autoinhibition and regulation of NHE9. (A)** Numerous contacts are formed between the CTD and the linker helix TM7 (depicted as side view right; depicted as top view left (shown in cartoon, colored as in Figure 1A). **(B)** In the horse NHE9* CC structure the CTD stays connected to the linker helix TM7 (protein shown as surface, colored as in Fig1A). **(C)** *above:* AF2 model of NHE1 predicts CTD interacts to TM7 as seen in the NHE9* CC cryo EM structure. *below:*Aligning the NHE9*CC structure (blue-salmon) with inward-facing human NHE1 CTD (grey) and CHP1 (green) **(D)** CHP1 (green, surface) binding to the CTD of NHE1 (grey, surface) moves it away from the linker helix TM7.

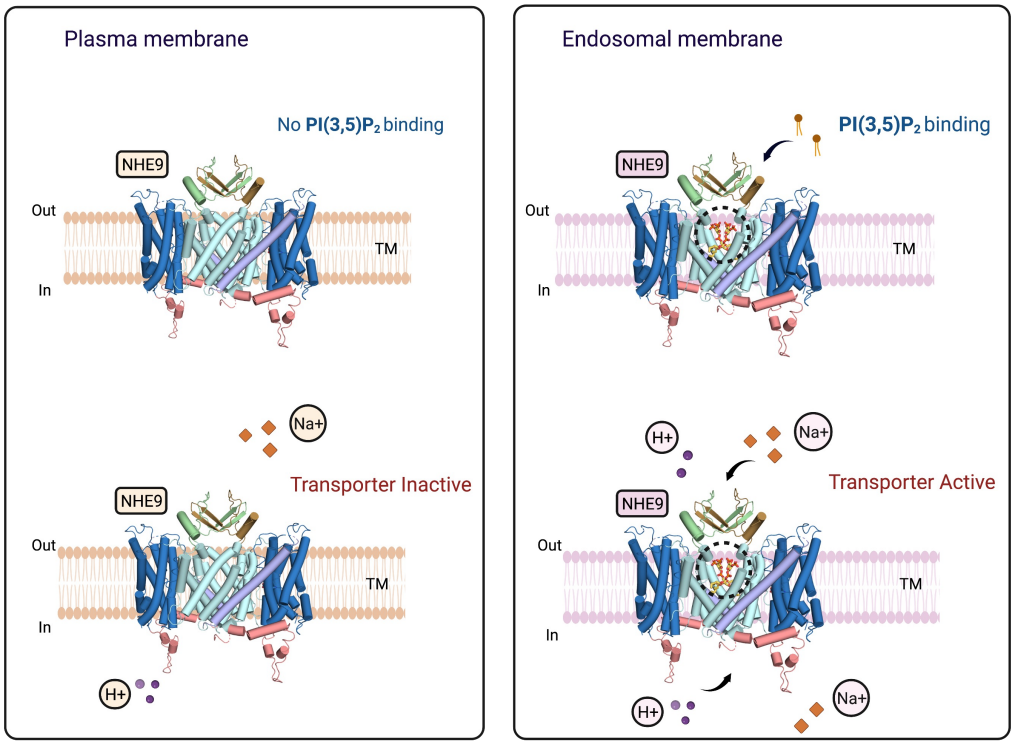


1102

1103 **Figure 7. The PI-(3,5)$P_2$-dependent activation of NHE9 in late endosomes.**
1104 Schematic representation of NHE9 ion translocation, dimer stabilisation and transport
1105 activation in the endosomes vs. the cell membrane. NHE9 is inactive in the plasma
1106 membrane. Upon relocation into late endosomes, a concomittant bindning of PI-(3,5)$P_2$
1107 at the dimerization interface improves the stability of homodimer and activates the
1108 transporter. The figure was created using Biorender.com